Experimental demonstration of a Maxwell's demon quantum battery in a superconducting noisy intermediate-scale quantum processor

Jiale Yu,[1,2,3,*] Shiyu Wang,[1,2,3,*,†] Kangqiao Liu,[4] Chen Zha,[1,2,3] Yulin Wu,[1,2,3] Fusheng Chen,[1,2,3] Yangsen Ye,[1,2,3] Shaowei Li,[1,2,3] Qingling Zhu,[1,2,3] Shaojun Guo,[1,2,3] Haoran Qian,[1,2,3] He-Liang Huang,[1,2,3] Youwei Zhao,[1,2,3] Chong Ying,[1,2,3] Daojin Fan,[1,2,3] Dachao Wu,[1,2,3] Hong Su,[1,2,3] Hui Deng,[1,2,3] Hao Rong,[1,2,3] Kaili Zhang,[1,2,3] Sirui Cao,[1,2,3] Jin Lin,[1,2,3] Yu Xu,[1,2,3] Cheng Guo,[1,2,3] Na Li,[1,2,3] Futian Liang,[1,2,3] Gang Wu,[1,2,3,5] Yong-Heng Huo,[1,2,3] Chao-Yang Lu,[1,2,3] Cheng-Zhi Peng,[1,2,3] Kae Nemoto,[6] W. J. Munro,[6,‡] Xiaobo Zhu,[1,2,3] Jian-Wei Pan,[1,2,3] and Ming Gong[1,2,3,§]

[1]*Hefei National Research Center for Physical Sciences at the Microscale and School of Physical Sciences, University of Science and Technology of China, Hefei 230026, China*

[2]*Shanghai Research Center for Quantum Science and CAS Center for Excellence in Quantum Information and Quantum Physics, University of Science and Technology of China, Shanghai 201315, China*

[3]*Hefei National Laboratory, University of Science and Technology of China, Hefei 230088, China*

[4]*School of Science, Key Laboratory of High Performance Scientific Computation, Xihua University, Chengdu 610039, China*

[5]*University of Science and Technology of China, Shanghai Research Institute, Shanghai 201315, China*

[6]*Okinawa Institute of Science and Technology Graduate University, Onna-son, Okinawa 904-0495, Japan*

(Received 9 February 2024; revised 2 May 2024; accepted 24 May 2024; published 20 June 2024)

Entering the era of post-quantum supremacy has given one the ability to precisely control noisy intermediate-scale quantum (NISQ) processors with multiqubits and extract valuable quantum many-body correlation resources for many distinct quantum applications. We here construct quantum many-body thermalized states on a 62-qubit superconducting quantum processor and use them to demonstrate the principle of Maxwell's demon. We further demonstrate the direct effect caused by Maxwell's demon on the charging process of a quantum battery (QB). We depicted the nonequilibrium transportation in our QB through measuring the dynamics of the Shannon entropy to explore its working conditions. Finally, we evaluate the information-to-work conversion by varying the readout fidelity to verify the validity of the Sagawa-Ueda equality within the NISQ processor environment and evaluate the qubit-environment interaction such as the measurement backaction. Our experiment suggests that the superconducting NISQ processor with appropriate error mitigation methods will be an ideal platform for studying quantum information thermodynamics through quantum many-body simulations.

DOI: 10.1103/PhysRevA.109.062614

I. INTRODUCTION

In the mid-19th century Maxwell conceived a thought experiment that could hypothetically violate the second law of thermodynamics [1]. A demon (Maxwell's demon) would control a small door between two atom-filled chambers such that the door opens only for fast-moving atoms to pass through in one direction and slow-moving ones in the other. Over time, one chamber heats up while the other cools down as shown schematically in Fig. 1(a). This violation of the second law of thermodynamics as the entropy of the total system decreases has been solved by introducing Landauer's principle [2], which states that erasing information also needs work. Maxwell's demon has been implemented experimentally in various quantum systems including NMR systems [3], photonic systems [4], single-electron transistors [5,6], neutral atoms [7,8], and few-qubit superconducting systems [9–12]. These experiments have provided a deeper understanding of the relationship between quantum information and thermodynamics—spawning the new field of quantum thermodynamics [13,14]. On the other hand, quantum batteries (QBs) [15–20] assisted by measurement and feedback control [21–25] extend the application scenarios of Maxwell's demon in quantum thermodynamics even further.

Thermodynamics is generally built around the concept of equilibrium states involving multiple particles, and this was especially true of the original Maxwell's demon thought experiment. The recent experimental exploration of Maxwell's demon in the quantum regime has generally been limited to few-qubit systems or the rearrangements of particles on the fixed lattice. However, when it comes to multiqubits, urgent attention is required for the investigation within the quantum many-body regime due to unique many-body features such as the eigenstate thermalization hypothesis (ETH), which states that a nonintegrable isolated quantum many-body system thermalizes for any initial state [26–31]. Therefore, quantum many-body systems are beneficial for experimentally studying quantum information thermodynamics.

The focus of our article will be to investigate a quantum battery (QB) assisted by Maxwell's demon operated within a quantum many-body system formed from a 62-qubit

*J.Y. and S.W. contributed equally to this work.

†Present address: RIKEN Center for Quantum Computing (RQC), Wako, Saitama 351-0198, Japan.

‡Contact author: bill.munro@oist.jp

§Contact author: minggong@ustc.edu.cn

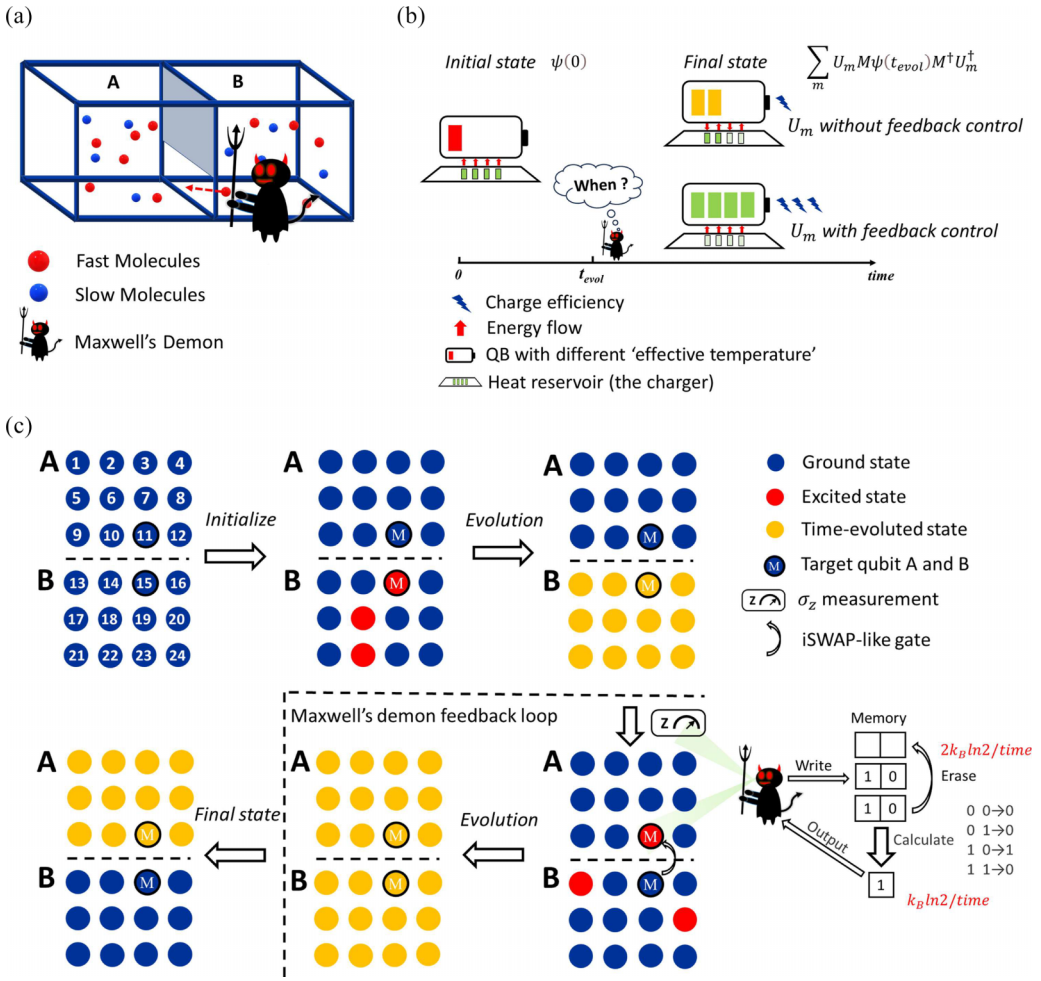

FIG. 1. (a) Schematic illustration of the Maxwell's demon thought experiment where the demon extracts work and controls heat transfer direction [38] through information of the microscopic state in gas molecules. (b) The application of Maxwell's demon in the QB scenario. The Maxwell's demon should choose a reasonable time when charging the battery. (c) Schematic diagram of Maxwell's demon with the 2D superconducting qubit processor to move the excitation gradually from subsystem B to A. The bottom layer of Maxwell's demon includes erase, write, logic operation, and result classification, where erasing the last information with an irreversible logic operation will increase the entropy cost [40]. The processing method of measurement outcomes by Maxwell's demon determines that the entropy cost in our feedback protocol is still bounded by the Landauer limit.

superconducting quantum processor [32]. Using quantum error mitigation method [33], our NISQ processor is programmable under accurate control with an efficient readout of every single qubit, which provides the ability to construct interaction adjustable systems of different scales, thus providing an excellent platform for exploring quantum many-body systems with Maxwell's demon. So we study experimentally the stored work after charging a QB through Shannon entropy dynamics to evaluate the working conditions of QB in Fig. 1(b) and measure the information-to-work conversion efficiency to verify the Sagawa-Ueda equality [34], namely, the fluctuation theorem valid for Maxwell's demon under NISQ environment and sequential measurements [35–37].

II. EXPERIMENTAL APPROACH

As a many-body generalization of the single-qubit experiment done in Ref. [11], the concept behind our experiment is depicted in Fig. 1(c). We implement two mutually isolated 3×4 qubit array subsystems A and B without coupling to an external heat bath. We mention that Maxwell's demon with an isolated working agent rectifies *pure quantum* fluctuations rather than the conventional thermal fluctuations, and this feature is unique to a *genuinely* quantum Maxwell's demon, which has attracted more and more attention [22,25,38]. The Hamiltonian of each subsystem is approximately a 2D hard-core Bose-Hubbard model, thus ensuring the ETH while the system size is large enough (larger than 3×4 for our case). Due to the ETH, Maxwell's demon with a larger size can be regarded as rectifying thermal fluctuations because they cannot be distinguished from quantum fluctuations.

We divide our 2D superconducting qubit array into two subsystems labeled as A and B, in analogy to the two chambers in the original Maxwell's thought experiment shown in Fig. 1(a). As shown in Fig. 1(c), the feedback loop is designed as follows. (1) The initial state of subsystem A is prepared to be the ground state while that of B contains several excitations. (2) We let both subsystems undergo unitary

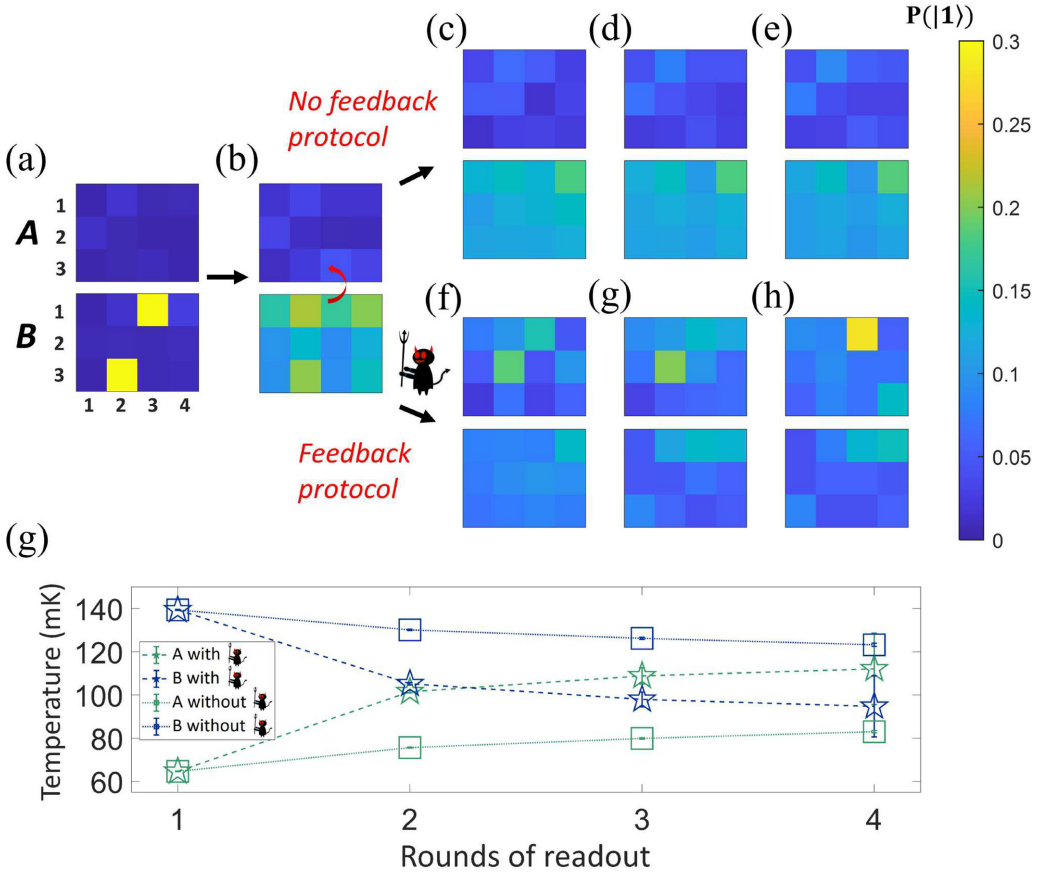

FIG. 2. The energy transfer process from subsystem B to subsystem A of size 3×4 each round. (a) The initial state of the total system where two qubits were excited. (b) The σ_z measurement probability distribution using 3 million results of each qubit after evolution. (c)–(h) Plots of the probability distributions after round 2, 3, 4 without or with the action of Maxwell's demon, respectively. In (c)–(e) we use an iSWAP gate to connect the subsection without the feedback protocol, while in (f)–(h) we use Maxwell's demon qubits that are measured with only the $|0\rangle$ state for target qubit A and $|1\rangle$ state for target qubit B being retained. (g) The temperature in different rounds of each subsystem.

time evolution in an isolated manner for a fixed time period t_{evol}. (3) Next, we realize σ_z projective measurements on every qubit independently and simultaneously with two-point measurement (TPM) protocols using sequential dispersive measurements [39] to determine the state of the subsystems $\xi_1 \otimes \xi_2 \otimes \cdots \xi_n$, where $\xi_i \in 0, 1$. (4) If "q11" (labeled as target qubit A) is found to be 0 and "q15" (labeled as target qubit B) is found to be 1, we swap them through the two-qubit iSWAP gate selectively. We then start the next cycle with this final state being the new initial state. Full details are described in the Appendixes.

III. DEMONIC EFFECTS

We explore the effect of Maxwell's demon on the QB by running k feedback loops for k qubits excited initially. Postselection is used to keep only events where the total excitation number is conserved in this experiment. The error of swap operation is 0.025 with swapping time 105 ns. The average readout fidelity of the qubit for $|0\rangle$ and $|1\rangle$ is 0.954 and 0.909 respectively. For a single isolated qubit, we define the "effective temperature" as $T_s = \hbar\omega_q/[k_B \ln(P_0/P_1)]$ and occupation number as $n_s = 1/\{1 + \exp[\langle \hat{H}_s \rangle/(k_B T_s)]\}$ where $\omega_q/2\pi$ is the frequency of the qubits, k_B is the Boltzmann constant, $\langle \hat{H}_s \rangle$ is the energy level, and $P_{0,1}$ the probabilities of qubits being in the $|0, 1\rangle$ state respectively [11]. For N qubits, to quantify the energy level in a many-qubits system, the average "effective temperature" T_{ave} can be defined according to the mean photon number $\sum_j n_j/N$,

$$T_{\text{ave}} = \hbar\omega_j \Big/ \left\{ k_B \ln \left[N \Big/ \left(\sum_j n_j \right) \right] - 1 \right\}, \qquad (1)$$

where n_j is the occupation number for the jth qubit (details are shown in the Appendixes).

To be specific, in Fig. 2, we show the dynamics of our Maxwell's demon QB beginning in Fig. 2(a) by exciting two qubits (1,3) and (3,2) in subsystem B. Then we wait for an appropriate period of time for those excitations to be more uniformly distributed in B by unitary evolution as shown in Fig. 2(b). The temperatures of A and B after the subsystem thermalizes are 65 mK (due to environmental thermal excitations and readout errors) and 139 mK, respectively. The acceleration of energy flow between two subsystems by Maxwell's demon can be understood as follows. If there is no feedback control, namely, if we always switch on the iSWAP gate on the two target qubits regardless of the measurement results, then in the second round [Fig. 2(c)], the iSWAP gate allows a small amount of energy (excitations) to flow from

B to A, and the temperature of A rises to 76 mK while that of B decreases to 130 mK. On the other hand, a significantly larger amount of energy is transferred to A from B through the feedback control in [Fig. 2(f)], causing the probability distributions of the excitation numbers of A and B to become close to each other. The temperatures of A and B are now 102 mK and 105 mK respectively. The effect of Maxwell's demon is even more significant in the third and fourth rounds. The energy flow without feedback control is still small resulting in the temperature of 80 mK in A, 126 mK in B in the third round and 83 mK in A, 123 mK in B respectively in the fourth round. However, the situation is very different under feedback control shown in Figs. 2(g) and 2(h), where the excitation number of A has exceeded B with the temperature of A being 109 mK and B being 98 mK in the third round and A at 112 mK, B at 95 mK in the fourth round. Finally, subsystem A is 17 mK higher than B. It's clear that the feedback protocol has significantly accelerated the heat-transport process from B to A and even can pump heat from a lower-temperature system to a higher-temperature one if we considered the temperature reversal phenomenon between A and B.

IV. QB WORKING CONDITIONS

Next, we explore the suitable time to start the feedback control in our QB with different system sizes from the perspective of thermodynamics. For a QB with multiqubits, researchers have found that the dynamic ergodicity [41] is highly correlated with its *ergotropy*, which is a key indicator [42–47] to evaluate its work extraction capabilities. To depict this nonequilibrium transportation process, we use the Shannon entropy of the state after charging our QB to describe the ergodicity. So we define

$$\eta_{\mathrm{Sh}}(t_{\mathrm{evol}}, r) = \frac{S_{\mathrm{Sh}}(t_{\mathrm{evol}}, r) - \max[S_{\mathrm{Sh}}(r-1)]}{\max[S_{\mathrm{Sh}}(r)] - \max[S_{\mathrm{Sh}}(r-1)]} \qquad (2)$$

to calculate the ratio of the stored work to the *ergotropy* occupied in phase space after the feedback loops, where r is rounds of readout. The maximum entropy $\max[S_{\mathrm{Sh}}(r)] = \log_2 C_n^{r-1}$ corresponds to the maximum number of microstates $\mathbf{\Omega}$ reconstructed by Shannon entropy through $\mathbf{\Omega} \to \mathbf{E}$ in phase space, C_n^{r-1} is the dimension of the Hilbert space in the rth readout, and n is the number of qubits.

In our setup, we executed the quantum circuit corresponding to Fig. 1(c) with different t_{evol} and various system sizes to observe the dynamical behavior of $\eta_{\mathrm{Sh}}(t_{\mathrm{evol}}, r)$. The results are shown in Fig. 3 for the 2×2 1D periodic chain and 3×4 2D lattice (while 2×3 and 3×3 sizes are shown in the Appendixes). We also tested the same conditions when the iSWAP gate is closed (background test). Our results show that the postselection rate of background is obviously smaller, indicating that most of the measurements are certainly driven by Maxwell's demon (see the Appendixes).

In Figs. 3(a) and 3(b), we plot η_{Sh} vs t_{evol} for the 2×2 and 3×4 subsystem sizes, respectively. We clearly observe significant oscillations for the 2×2 subsystem while the 3×4 subsystem almost stabilizes in the range 0.8–0.93. Further, the averaged value $\overline{\eta_{\mathrm{Sh}}(t_{\mathrm{evol}}, r)}$ in subsystem 2×2 after 50 ns is much lower than that in subsystem 3×4. It is also noticeable that $\overline{\eta_{\mathrm{Sh}}(t_{\mathrm{evol}}, 3)} < \overline{\eta_{\mathrm{Sh}}(t_{\mathrm{evol}}, 2)}$ in both subsystem

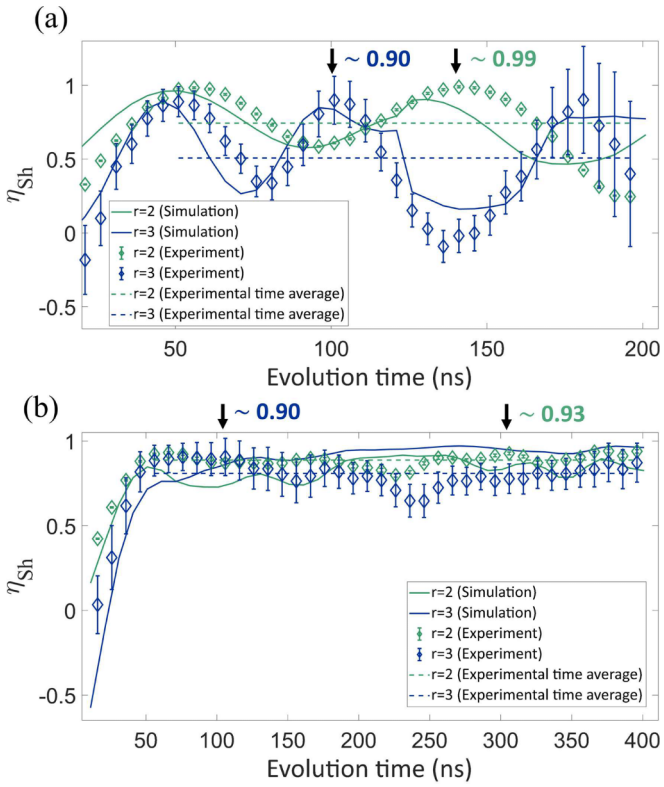

FIG. 3. Dynamics of the Shannon entropy rate related to maximum entropy η_{Sh} in the Maxwell's demon QB for subsystem $2 \times 2A$ and $3 \times 4A$ in (a) and (b) respectively. The averaged values in (a) after 50 ns are 0.744 and 0.508 for $r = 2$ and $r = 3$, respectively, while those in (b) are 0.888 and 0.809, respectively. The maximum peak values of experimental data are noted with corresponding colors. Also shown with solid lines are the results from the numerical simulation. Full details are given in the Appendixes.

sizes, reflecting the fact that the acceleration effect in the heat-transport process is easier to achieve than the effect of the heat-pumping process. Finally, it seems that η_{Sh} is strongly influenced by the finite-size effect. An intuitive understanding may be that the small-size system never thermalizes and remains out of equilibrium. The rectification of fluctuations is harder than a larger system. As a conclusion, the result suggests that a QB with a higher degree of thermalization seems better for charging stability, while a QB with a smaller size might be a better choice of a higher η_{Sh} (nearly 0.99) with an appropriate operation time. We also explored various other metrics such as Kullback-Leibler divergence [48], Krylov complexity [49,50], and Kolmogorov-Sinai entropy [51] to finely characterize the ergodicity inside the QB as supporting materials. These are presented in the Appendixes.

V. INFORMATION-TO-WORK CONVERSION

We finally evaluate the information-to-work conversion efficiency and test the Sagawa-Ueda equality [34,52,53], namely, $\langle e^{\beta(\Delta F - W) - I} \rangle = 1$ with $\langle W \rangle$ the useful work extracted from the heat reservoir and $\langle I \rangle$ the average mutual information obtained by Maxwell's demon from the target qubit while $\beta = 1/(k_B T)$. The modified second law of thermodynamics

can be derived from the Sagawa-Ueda equality as $-(\langle W\rangle - \Delta F) \leqslant k_B T \langle I\rangle$. It means that the excess extractable work by Maxwell's demon is bounded from above by the mutual information gained in the measurement process.

Using our 3×3 subsystem, we initially excited one qubit in B and measured the target qubit B with different readout fidelity sequences to obtain different measurement error sequences (details are shown in the Appendixes). First, we investigate the modified second law. It is straightforward to show that $-\langle W - \Delta F\rangle$ of a quantum system is [5,54]

$$\langle \Delta F - W\rangle = \mathrm{tr}\left(\sum_m U_m M \hat{H} M^\dagger U_m^\dagger - \hat{H}\right)\rho \otimes P(|\xi\rangle), \quad (3)$$

where $|\xi\rangle$ is the initial state of subsystem, $P(|\xi\rangle)$ is the projection operator of $|\xi\rangle$, $\hat{H}$ the Hamiltonian of subsystem, M is the measurement operator with outcome $m \in \{0, 1\}$, and U_m is the conditional unitary evolution operator used in the feedback control. Previous work have shown that $\langle W_{\epsilon=0}\rangle$ can be measured by TPM protocol [55–58]. Specifically for subsystem A, the measurement error ϵ influences the $\langle \Delta F - W_A\rangle$, since the results of $|0\rangle$ will be incorrectly identified as $|1\rangle$. This can be recalculated as [59,60]

$$\langle \Delta F - W_A\rangle_{\epsilon=0} = k_B T_A\left[\ln 2 - \ln\left(1 + e^{-\frac{\Delta E_A}{k_B T_A}}\right)\right], \quad (4)$$

$$\langle \Delta F - W_A\rangle_{\epsilon} = \langle \Delta F - W_A\rangle_{\epsilon=0} - \epsilon_{1\to 0}\Delta E_A, \quad (5)$$

where $\Delta E_A = \sum_{i\in\{A\}} \Delta P_i h f_i$ is the energy change in subsystem A, determined from the probability change $\Delta P_i(|1\rangle)$ of each qubit in A, and T_A is the temperature of A at the second readout round. Now as seen in Fig. 4, $\langle \Delta F - W_A\rangle$ decreases when ϵ of Maxwell's demon qubit increases. We also notice that the information-to-work efficiency η has a maximal value as high as 88%, which is close to unity and much higher than previous experiments [11,53]. The reason is that the saturation of the modified second law is satisfied only by the Szilard-type engine that operates quasistatically while the systems in previous experiments are generally out of equilibrium. Differently, the ETH obeyed by our larger-size systems ensures near-equilibrium states, and the unitary evolution simply brings the subsystems to the new near-equilibrium states. Due to the limitations of the system size, the finite-size effect affects the thermalization to prevent the efficiency from being unity. Furthermore, $\beta\langle I\rangle$ decreases from Shannon entropy to 0 as the measurement error increases. Finally, the converted energy is always lower than the mutual information. Therefore, we have verified the validity of the modified second law of thermodynamics in our quantum many-body Maxwell's demon, and we have obtained a high information-to-work conversion efficiency compared with existing experiments.

Next, we verify the validity of the Sagawa-Ueda equality, which is more refined than the second law and also attractive experimentally [61,62]. We can then determine the mutual information between the target qubit B and the demon with different readout fidelity (details are shown in the Appendixes). We observe in Fig. 4(b) that without Maxwell's demon, $\langle e^{\beta(\Delta F - W_A)}\rangle$ decreases as the ϵ increases. Next we consider the mutual information I, $\langle e^{\beta(\Delta F - W_A) - I}\rangle$ doesn't fluctuate around 1 but 0.8 due to an additional reduction $\langle \hat{H}_{q-env}\rangle$ in ΔE_A which is not included in the original theory of the

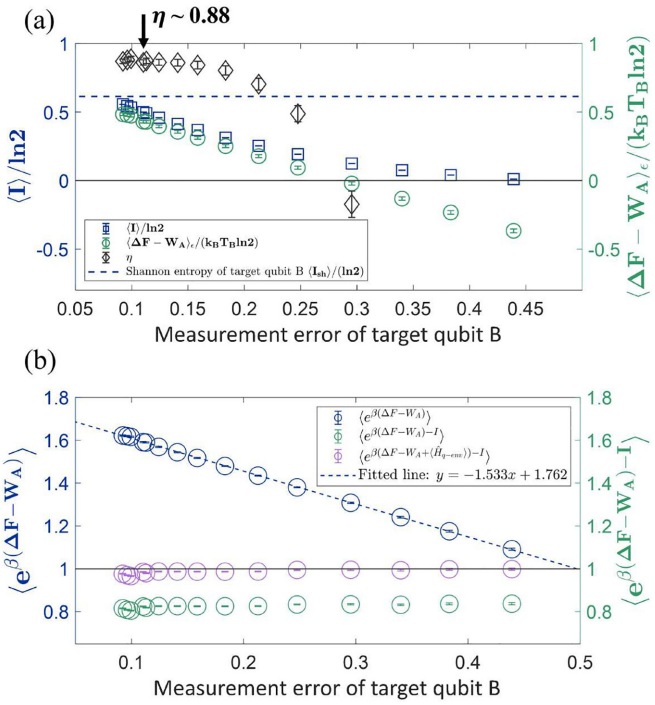

FIG. 4. Verification for the second law of thermodynamics and Sagawa-Ueda equality in a single-excitation quantum many-body environment. (a) Modified second law verification where the blue hollow square, dark green circle, and gray diamond dots show the relationship between mutual information $\langle I\rangle$, $\langle \Delta F - W_A\rangle$, and conversion efficiency $\eta = \langle \Delta F - W_A\rangle_\epsilon/(\beta\langle I\rangle)$ vs the measurement error of target qubit B. The blue dashed line shows the Shannon entropy of target qubit B, $S(t_{\mathrm{evol}}) \sim 0.613 \ln 2$, which is the upper bound of $\langle \Delta F - W_A\rangle$. (b) The Sagawa-Ueda equality where the dark blue, green, and purple circles plot $\langle e^{\beta(\Delta F - W_A)}\rangle$, $\langle e^{\beta(\Delta F - W_A) - I}\rangle$, and $\langle e^{\beta(\Delta F - W_A + \langle \hat{H}_{q-env}\rangle) - I}\rangle$, respectively.

Sagawa-Ueda equality. When we include our experimental data $\langle \hat{H}_{q-env}\rangle$ in the exponent, specifically the measurement backaction ($0.283\ k_B T_A$), the decoherence ($-0.086\ k_B T_A$), and the thermal excitations ($0.517\ k_B T_A$), $\langle e^{\beta(\Delta F - W_A + \langle \hat{H}_{q-env}\rangle) - I}\rangle$ fluctuate near 1. Hence, if we take the qubit-environment interaction into account, we have verified the validity of the Sagawa-Ueda equality.

VI. CONCLUSION AND OUTLOOKS

In this work, we have demonstrated Maxwell's demon-type QB on a NISQ processor, which has extended the application of quantum correlation resources [21,63–66] into new NISQ regimes [67]. In particular, using a 2D superconducting array divided into two subsystems each containing 12 qubits, we explored the Shannon entropy dynamics after charging one of the subsystems (the battery) with Maxwell's demon, and studied the information-to-work conversion mechanism under qubit-environment interaction. It turns out that our NISQ processor with appropriate error mitigation methods is an ideal platform for investigating quantum information thermodynamics, especially the many-body systems in which many unique features [30,68,69] arise such as the ETH or

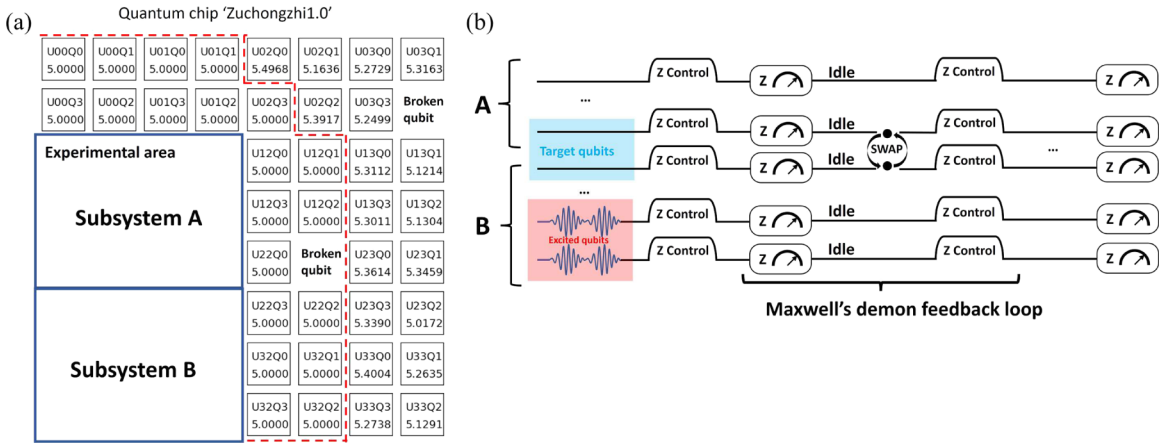

FIG. 5. (a) Layout of the qubits in experimental area of the quantum processor where the numbers under qubit in the nonexperimental area are frequency in GHz. Red dashed line marks the proximity and subproximity qubits of experimental area, which are biased to 5.0 GHz. Qubits outside of the red dashed line were not used in this experiment. (b) The waveforms corresponding to each step in Fig. 1(c).

finite-size effects which help us study the conventional Maxwell's demon even using a pure quantum system.

The high programmability of our NISQ processor may also allow scaling up to implement a macroscopic quantum Maxwell's demon which is extremely nontrivial even for classical systems [70]. We can also explore how our system can be used to both build a quantum heat machine [71,72] as well as extract entropy from a system as a means to perform quantum error correction [73–75]. The relationship between Maxwell's demon and integrability [76–79] might be an intriguing question as well.

ACKNOWLEDGMENTS

The authors thank Zheng-Hang Sun, Shoki Sugimoto, and Hai-Long Shi sincerely for useful suggestions on ETH and QB. The authors appreciate Zongping Gong and Haoyu Guan for fruitful discussions. The authors thank the USTC Center for Micro- and Nanoscale Research and Fabrication for supporting the sample fabrication. The authors also thank QuantumCTek Co., Ltd. for supporting the fabrication and maintenance of room-temperature electronics. This research was supported by the Innovation Program for Quantum Science and Technology (Grant No. 2021ZD0300200), Shanghai Municipal Science and Technology Major Project (Grant No. 2019SHZDZX01), Chinese Academy of Sciences, Anhui Initiative in Quantum Information Technologies, Technology Committee of Shanghai Municipality, Natural Science Foundation of Shanghai (Grant No. 19ZR1462700), and special funds from Jinan Science and Technology Bureau and Jinan High Tech Zone Management Committee. K.L. was supported by the Scientific Research Start-up Foundation of Xihua University (Grant No. Z241064). H.-L.H. acknowledges support from the Youth Talent Lifting Project (Grant No. 2020-JCJQ-QT-030), National Natural Science Foundation of China (Grants No. 11905294, No. 12175003, and No. 12147133), China Postdoctoral Science Foundation, High-Performance Computing Platform of Peking University, Open Research Fund from State Key Laboratory of High Performance Computing of China (Grant No. 201901-01), and Zhejiang Lab's International Talent Fund for Young Professionals. M.G. was supported by the National Science Foundation of China (Grant No. T2322024), Shanghai Rising-Star Program (Grant No. 23QA1410000), and the Youth Innovation Promotion Association of CAS (Grant No. 2022460). X.B.Z. acknowledges support from the Xplorer Prize.

APPENDIX A: BASIC PARAMETERS OF QUANTUM PROCESSOR

We use a superconducting qubit-based quantum possessor as shown in Fig. 5(a) to demonstrate the Maxwell's demon experiment. Here the quantum processor was cooled to 20 mK using a BlueFors XLD400 [32]. The processor consists of a 8×8 array of 64 qubits, two of them are nonfunctional. Each qubit has a separate readout cavity and an *XYZ* control line, while every four qubits share a readout filter and line. Next every two adjacent qubits are coupled to each other through a $\lambda/2$ coplanar waveguide resonant cavity. Given that processor layout in our experiment we use 24 qubits located in the lower left corner of the processor away from the nonfunctional ones configured as a two-dimensional array of 4×6 containing six readout units. The coupling between U10Q0 and U10Q3 is disabled.

The characterization parameters of the 24 qubits are shown in Fig. 6 and summarized in Table I.

APPENDIX B: SYSTEM CALIBRATION PROCESS

The key steps in our Maxwell's demon demonstration are as follows:

(i) *Step 1, Initialization:* The experimental qubits array are divided into two parts: subsystem A and B where we excite several qubits in B to prepare our initial state. U21Q0 (labeled as target qubit A) and U21Q3 (labeled as target qubit B) are selected as the target qubits of the two subsystems A and B, respectively. All qubits are biased to the idle frequency by Z control. The *XY* microwave drive pulse should regulated to 40–45 ns for multiqubit timing alignment.

(ii) *Step 2, Evolution:* Subsystem A is aligned at 5.2 GHz while B is aligned at 5.13 GHz to evolve for a time t_{evol}, respectively.

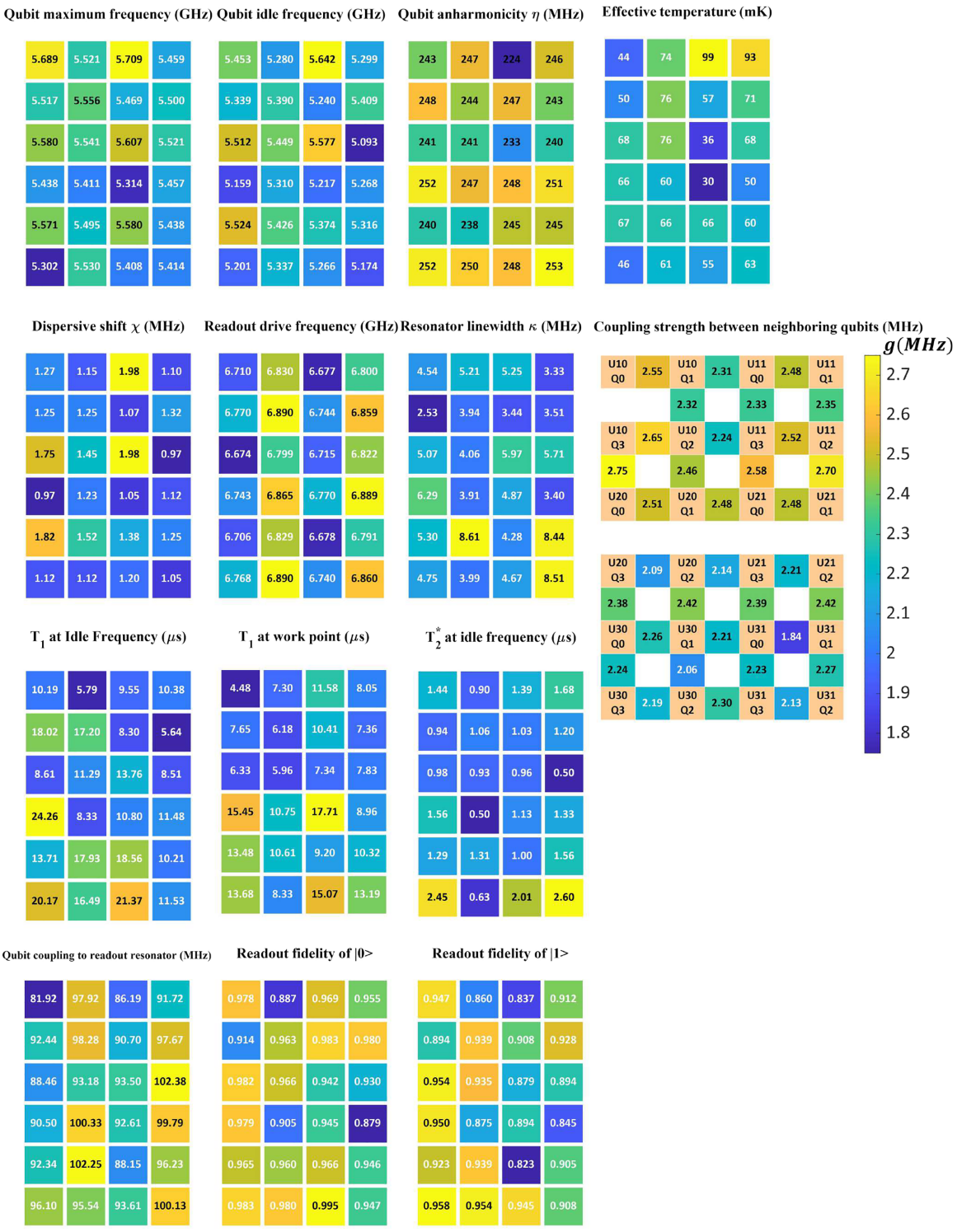

FIG. 6. Qubit parameter distributions, including qubit maximum frequency, qubit idle frequency, anharmonicity, dipersive shift, qubit readout drive frequency, resonator line width, readout fidelity, coupling strength between qubit and resonator, qubit energy relaxation time T_1 at the idle/work point, qubit dephasing time T_2^* at the idle point, effective temperature, and distribution of the coupling strengths between neighboring qubits. Each square in the diagrams represents a qubit; the number and color in the square show the value of the corresponding parameter. The square connecting two qubits shows the effective coupling strength between them when these two qubits are tuned to the interaction frequency of 5.13 GHz in subsystem A and 5.2 GHz in subsystem B.

TABLE I. Statistics of qubit parameters.

Parameters	Median	Mean	Std. dev.
Qubit maximum frequency (GHz)	5.508	5.501	0.099
Qubit idle frequency (GHz)	5.326	5.344	0.137
Qubit anharmonicity $\eta/2\pi$ (MHz)	245.7	244.4	6.5
T_1 at idle frequency (μs)	11.4	13.0	5.1
T_1 at work frequency (μs)	9.1	9.9	3.4
T_2^* at idle frequency (μs)	1.2	1.3	0.5
Coupling strength between qubit and readout resonator (MHz)	93.6	94.2	5.2
Effective coupling strength between neighboring qubits (MHz)	2.3	2.3	0.2
Half of dispersive shift $\chi/2\pi$ (MHz)	1.2	1.3	0.3
Readout drive frequency (GHz)	6.781	6.784	0.071
Resonator line width $\kappa/2\pi$ (MHz)	4.7	5.0	1.6
Readout fidelity of $\|0\rangle$	0.964	0.954	0.031
Readout fidelity of $\|1\rangle$	0.910	0.909	0.039
Effective qubit temperature (mK)	64.5	62.6	15.8

(iii) *Step 3, Measurement:* The σ_z projection is measured for all qubits by cavity readout, and the one-state dispersive shift method is strictly used in the data acquisition in order to reduce the effect of high energy leakage.

(iv) *Step 4, Swap operation:* Our two target qubits are biased to 5.15 GHz by Z to construct the iSWAP gate. In this experiment, the coupling strength of the two target qubits is 2.323 MHz, while the duration of the iSWAP gate is 120 ns. Cross-entropy benchmarking (XEB) shows a gate fidelity is 99.21%.

Steps 2, 3, and 4 are repeated $n + 1$ times with the continuous readout technique. No swap operation is performed for the last time, and the system is measured directly after evolution. Considering the AC stark shift, we wait 125 ns after each readout (except the last round) to control qubits again. Next let us give a few more details about the calibration process beginning with our system preparation.

1. Preparation

Before arranging the idle points of qubits we need to determine the relationship between f01 and z-bias for all the qubits. Here we selected 24 qubits in the lower-right orientation of the qubit processor as our experimental zone. To reduce the coupling or crosstalk effect brought by qubits outside this zone, we apply a bias to the proximity and subproximity qubits of the experimental zone to 5.0 GHz, as shown in Fig. 5(a).

2. Determining the idle point

After our basic qubit calibration, we need to determine the idle points of those qubits. To minimize the coupling effects of qubits due to their frequency proximity, all the qubits idle points in the experimental zone need to be determined. According to the energy spectrum's decoherence time T_1 variation with z-bias and with a circuit duration for the Maxwell's demon experiment of about 0.5 ms per cycle, we select all frequency point where T_1 is greater than 5 ms (10 times the Maxwell's demon cycle time) as alternative points. We then filter those points according to the following rules: The idle frequency of the qubits is staggered by more than 50 MHz, but avoids 234–250 MHz because of the two-level qubit state. Further the maximum frequency difference should not exceed 310 MHz. Next the secondary proximity coupling qubits are staggered by more than 10 MHz while the diagonal proximity coupling qubits are staggered by more than 30 MHz. After the above steps, we get an initial set of idle points for every qubit in our experimental zone.

We need to remember that the solution of idle points is not unique, and so the performance parameters such as T_1, T_2^*, readout fidelity for our experimental qubits need to be verified one by one. If there are any problems caused by TLS, defects, or electromagnetic pattern caused by slotted line, etc., this qubit is unqualified. Then we adjust the unqualified qubit and its adjacent and subadjacent qubits to find a new idle frequency. We then recalibrate the qubits and repeat the scheduling until all qubits at the idle frequency meet the experimental requirements.

After establishing the appropriate idle frequencies, the next procedure is associated with readout optimization and z-pulse distortion correction for all the experimental qubits. The readout optimization process requires adjusting the parameter of readout pulse and *Josephson parametric amplifier* (JPA) to improve the readout fidelity as high as possible, while the z-pulse distortion correction requires calibrating the additional phase generated by the difference between the actual z-waveform and the standard square waveform to improve the accuracy of qubit control. Finally, the frequency, length and amplitude of the X gate and pulse shaping through *derivative reduction by adiabatic gate* (DRAG) of all qubits are carefully performed. When the above steps allow to reach $\overline{F_{00}} > 0.95$ and $\overline{F_{11}} > 0.90$ we can move to the next stage: the frequency alignment process.

3. Frequency alignment and optimization

To allow subsystems A and B to evolute independently, we align the qubit frequencies within subsystems A and B respectively. Subsystem A is set to 5.13 GHz, while B is set to 5.2 GHz. Since there is inevitably small detuning amount caused by imperfect conditions, we eliminate such detunings by applying a correction to the frequency of each qubit. As

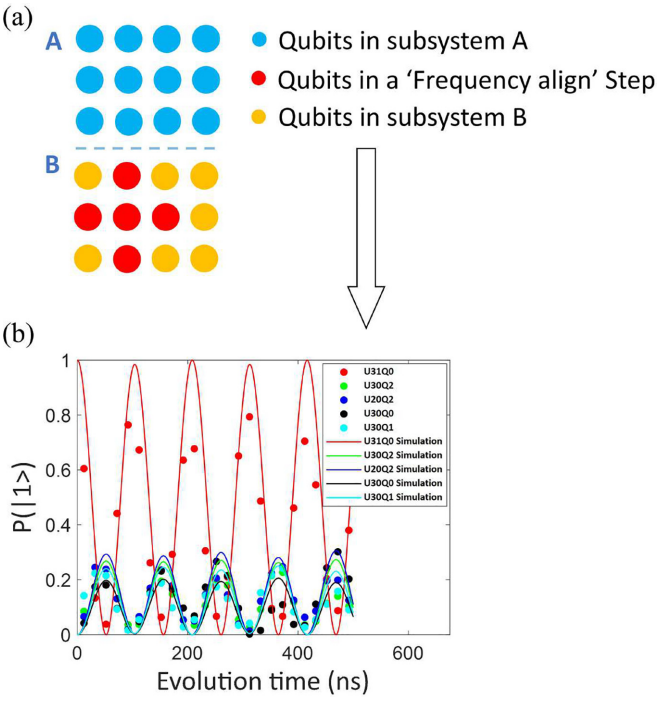

FIG. 7. Schematic diagram of our subsystem frequency alignment process. (a) One step of the subsystem B frequency alignment process for qubits U30Q1, U30Q2, U20Q2, U30Q0, U31Q0, where the excited qubit marked with red is U30Q1. (b) Experimental and simulated value of the probabilistic evolution of the qubits in (a). This is the basis for calculating the distance and updating the frequency correction matrix.

such the purpose of frequency alignment is to determine the size of this correction that needs to be applied to each qubit relative to the frequency alignment point. To measure the size of this detuning, the qubits in subsystems A and B are coupled in groups of two at 5.2 GHz and 5.13 GHz, respectively, while the remaining qubits are biased by 70 MHz to measure the coupling strength between those two qubits. Then we apply a correction value based on the actual frequency of the two qubits at the maximum coupling strength point.

Let us take subsystem A as an example. We choose an initial qubit and select its adjacent qubit. Then we excite one of them to the one state to measure the experimental value of the probabilistic evolution of the qubit for 500 ms. We then calculate the simulated value under the same conditions (the qubit coupling strength is known), noting that the disorder of qubits is calculated according to the Neld-Mead algorithm. The distance between the experimental simulated values is then defined as the sum of the squares of the differences between the data points of all the experimental and simulated values, as shown in Fig. 7. The qubit is adjusted one after another though this method with the new disorder of this qubit being updated. The above schedule is repeated until all the qubits in subsystem A are covered. We continue updating qubits until the distance does not change obviously with increasing the number of rounds. At this stage we stop the optimization.

Finally, each qubit forms a group with its upper, lower, left, and right four qubits. The number of groups is reduced accordingly for the qubits at the boundary. At this point the same test evolution of another qubit with the remaining unregulated qubits in the adjacent qubits is also carried out for 500 ms for the experimental value and the simulation value under the same conditions to obtain the highest to 55 group of qubits disorder matrix with distance. The value of this matrix will be used as the initial disorder matrix for a numerical simulation process.

For subsystem B, the above operation is also performed. As crosstalk between qubits located in the boundary of subsystem A and subsystem B, the correction of the Z pulse waveform in subsystem A will affect subsystem B to a certain extent. Similarly, the correction of the Z pulse waveform in subsystem B will also affect subsystem A. This means those qubits at the boundary need to be handled carefully, and it's necessary to fine-tune the frequency correction matrix of optimized subsystems A and B several times repeatedly and alternately.

Since this frequency alignment process is never perfect, we terminate the frequency alignment process when both subsystems A and B are able to describe the multiqubit system dynamics entropy property accurately with a higher ETH degree for larger system. Meanwhile, one to two qubits of the subsystem can be selected for excitation at any time during the frequency alignment process to observe the probabilistic evolution of the system and ensure that every qubit is involved in the evolution process.

4. Maxwell's demon parameter optimization

The main parameters during Maxwell's demon experiment are the swap frequency f_{swap}; the swap time t_{swap} required for the target qubits to completely transfer the energy and the waiting time t_{wait} after each Maxwell's demon readout operation because of AC stark effect. After the frequency alignment, these parameters should be optimized and the fidelity of the iSWAP gate composed of target qubits determined. The schematic diagram of each experimental circuit waveform for Maxwell's demon parameter calibration process in this section is shown in Fig. 8.

a. Optimization of t_{swap} and t_{wait}

Initially, we set the exchange frequency point for target qubits to 5.15 GHz while keeping the frequency point of U21Q0 unchanged. Exciting qubit U21Q3 to $|1\rangle$ we the conditional probability of U21Q0 being $|0\rangle$ under condition "U21Q3 is $|1\rangle$." According to the darkest color operating point in Fig. 9(a), the best exchange frequency and time for target qubits can be obtained. When running Maxwell's demon circuit, it is also necessary to fine-tune and optimize the frequency within the range of ± 3 MHz and exchange time within ± 5 ns according to the actual situation. We need to select the appropriate value to build the iSWAP gate and maximize the fidelity in the Maxwell's demon experiment. Finally, this experiment determines the target qubits exchange frequency point as U21Q0 for 5.1500 GHz, U21Q3 for 5.1567 GHz and the swap time as 105 ns.

Due to the AC Stark effect, the number of residual photons in the cavity from the last readout round has an effect on the qubit frequency, so after each readout (except the last round) it is necessary to wait for some time to let those residual

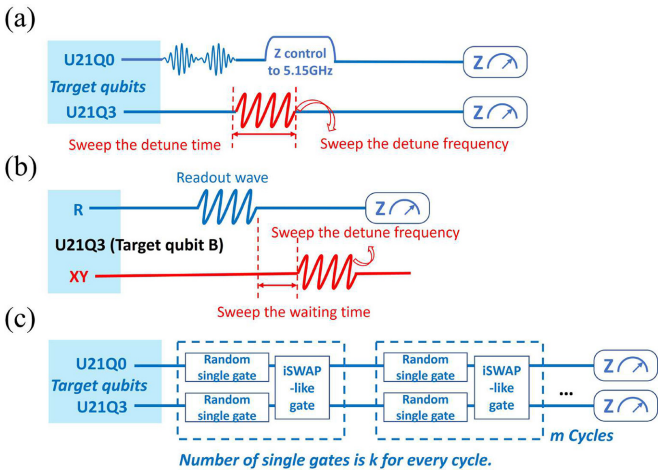

FIG. 8. Waveform schematic diagram of the each experimental circuit of the Maxwell's demon swap process parameters calibration process. (a) The waveform to determine the exchange operation frequency point between target qubits of the two subsystems. (b) The waveform to determine the shift of working point on target qubits after continues readout caused by AC Stark effect. (c) The waveform of the two-qubit gate XEB test for iSWAP gate composed of target qubits.

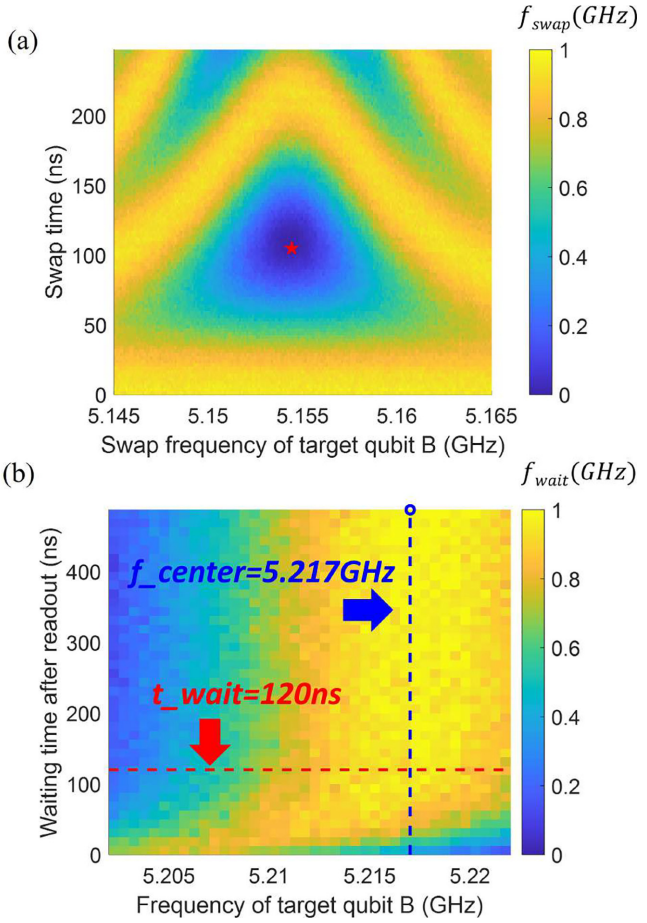

FIG. 9. (a) Calibration of time and frequency on target qubit B. The center of pentagram is the minimal value of P_{01}, which corresponds to the point with the best energy exchange. This point corresponds to the U21Q3 frequency of 5.1544 GHz with a swap time of 105 ns. (b) Calibration of the waiting time t_{wait} where we plot the frequency of U21Q3 vs t_{wait} after readout. Here the red dashed line is the marker line of 120 ns, while the blue dashed line marks the mean peak frequency value of U21Q3 (5.217 GHz).

photons in the cavity leak out before we control the qubits again. The waiting time t_{wait} is slightly higher than the time when the photon of readout cavity leakage to $1/e$ portion of initial count. Taking U21Q3 as an example, according to the blue dashed line in Fig. 9(b), U21Q3 is stable at 5.217 GHz with a half-peak width of ±4.13 MHz. The red dashed line is the dividing line between U21Q3 from being affected by the photon number in the cavity and the stable state. According to the Gaussian fitting results of the red dashed line in Fig. 9(b), the jitter of U21Q3 is 876.2 kHz, which is less than 1 MHz and meets the experimental requirements. The photon number decay of the remaining qubits is evaluated according to this way. Given this we set $t_{\text{wait}} = 125$ ns.

b. Fidelity calibration for the iSWAP gate

Next, we calibrate the iSWAP gate fidelity consisting of target qubits U21Q0 and U21Q3 according to f_{swap} and t_{swap} using the cross-entropy benchmarking (XEB) method. The two-qubit iSWAP gate belongs to the fermion universal two-quantum-qubit logic gate type characterized by photon number conservation. Its unitary matrix can be written as

$$\begin{bmatrix} 1 & 0 & 0 & 0 \\ 0 & \cos\theta & -i\sin\theta & 0 \\ 0 & -i\sin\theta & \cos\theta & 0 \\ 0 & 0 & 0 & e^{-i\phi} \end{bmatrix},$$

where θ is the swap angle and ϕ is the conditional phase. Since our experiments use transmon qubits and there is dynamic phase accumulation during the control process of qubit, we use five kinetic factors δ_+, δ_-, δ_{off}, θ, ϕ to fit the iSWAP gate [80,81],

$$\begin{bmatrix} 1 & 0 & 0 & 0 \\ 0 & e^{i(\delta_+ + \delta_-)}\cos\theta & -ie^{i(\delta_+ - \delta_{\text{off}})}\sin\theta & 0 \\ 0 & ie^{i(\delta_+ + \delta_{\text{off}})}\sin\theta & e^{i(\delta_+ + \delta_-)}\cos\theta & 0 \\ 0 & 0 & 0 & e^{i(2\delta_+ - \phi)} \end{bmatrix}.$$

In our experiments, the target qubits were first calibrated with a single-qubit gate sampled 100 times from eight random single-qubit gate groups $\pm X$, $\pm Y$, $\pm(X \pm Y)$, uniformly to obtain a single-qubit gate sequence, which was used to operate on the qubits for a single-qubit cycle operation. The experiments were performed in 18 groups, as shown in Fig. 8(c), and the number of cycles in each group was sequenced according to an exponentially increasing sequence $m = \{5\ 6\ 8\ 13\ 17\ 21\ 28\ 35\ 45\ 57\ 73\ 94\ 119\ 152\ 194\ 248\ 316\}$. Then we calculate the probability of theoretical value and measure the probability of the actual qubit under its corresponding operation.

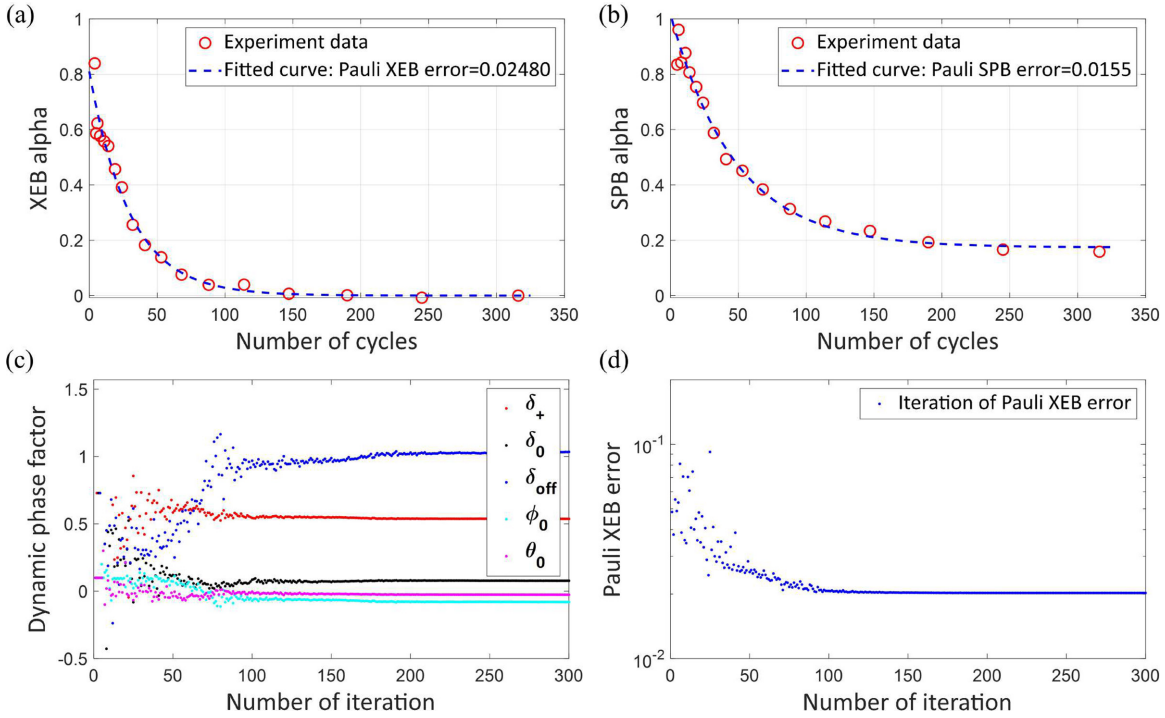

FIG. 10. Fidelity calibration of the iSWAP gate constructed by two target qubits. (a) The XEB alpha factor fitting procedure for a two-qubit gate constructed for target qubits. (b) The process of optimizing five kinetic phase factors using the Nelder-Mead method with Pauli XEB error as the objective function. (c) The variation of XEB error with the number of iterations during the optimization of the kinetic phase factors. (d) The iteration process of fitting the two-qubit iSWAP gate SPB alpha factor.

Using

$$\alpha_{\mathrm{XEB,singleQ}}(i) = \frac{1}{k}\sum_{m_i}\sum_{Pi} Pi_{\mathrm{exp,m_i}}[2^d(Pi_{\mathrm{theory,m_i}} - 1)] \quad \text{(B1)}$$

we can determine α for the ith set of XEB experiments where d is the Hilbert space dimension while Pi is the event kind composition (P0/P1 for a single qubit, P00/P01/P10/P11 for two qubits). Further k is number of samples (100 for the single-qubit gate sequence). Using the exponential model $Ap^m + B$ to fit α, where A is related to the initial state preparation error, B to the readout error, and p the Pauli XEB error we can determine that the XEB fidelity of the single-qubit gate constructed by target qubits is $1 - (2^d - 1)(1 - p)/2^d$. The Pauli error of target qubit A (U21Q0) is 0.0065, while target qubit B (U21Q3) is 0.0060.

After the calibration of the single qubit gates, we need to move to the two-qubit gate XEB testing to the validity of the results. The number of cycles and groups in each set are the same as in the single-qubit gate calibration process, but we now measure the target qubits 01 combination event probability P00/P01/P10/P11. Our two-qubit gate matrix containing the kinetic factor term is used to calculate the theoretical probability. The two-qubit gate factor α is given by

$$\alpha_{\mathrm{XEB,2Q}}(i) = \frac{1}{k}\sum_{m_i}\sum_{Pi} Pi_{\mathrm{exp,m_i}}[2^d(Pi_{\mathrm{theory,m_i}} - 1)]. \quad \text{(B2)}$$

Now through the Nelder-Mead algorithm, five kinetic factors δ_+, δ_-, δ_{off}, θ, and ϕ are iterated to optimize p and fit the exponential model $Ap^m + B$. The experiment was iterated 300 times, and the final solutions are $\delta_+ = 0.537$, $\delta_- = 0.078$, $\delta_{\mathrm{off}} = 1.034$, $\theta = -0.027$, $\phi = -0.081$ respectively, as shown in Fig. 10(c).

Now the total Pauli error is $e_{\mathrm{all}} = (2^d - 1)(1 - p)/2^d = 0.0248$. As shown in Fig. 10(a), Pauli error of target qubit A (U21Q0) equals 0.0065, while the Pauli error of target qubit B U21Q3 is 0.006. This means we get the iSWAP gate Pauli error as $e_{\mathrm{iSWAP}} = 1 - \frac{1-e_{\mathrm{all}}}{(1-e_{\mathrm{targetA}})(1-e_{\mathrm{targetA}})}$. Thus, the XEB fidelity of the two-qubit iSWAP gate is $1 - e_{\mathrm{iSWAP}} = 98.8\%$ with confidence interval 95%.

Further the error induced by decoherence effect on the two-qubit iSWAP gate is examined using the *Speckle purity benchmarking* (SPB) method. Defining the SPB coefficients

$$\alpha_{\mathrm{SPB}}(i) = \sum_{P_i} \mathrm{var}(P_i)\frac{2^{2d}(2^d + 1)}{2^d - 1}, \quad \text{(B3)}$$

the same fitting method was performed using the model $Ap^m + B$ giving the Pauli SPB error equals 0.0155 [as shown in Fig. 10(b)].

c. Postselection and the expectation of Maxwell's demon observation rounds

The expectation of Maxwell's demon observation rounds required per time can be determined using $n_{\mathrm{obs}}(r, t) = s(r - 1)/s(r)$, where $s(r)$ is the number of postselections in the rth round. The lower the value of n_{obs}, the easier is it that Maxwell's demon is triggered. As shown in Fig. 11, all systems have $n_{\mathrm{obs}}(3, t) > n_{\mathrm{obs}}(2, t)$.

If we use our feedback control directly without postselection, the circuit time increased by a single feedback operation

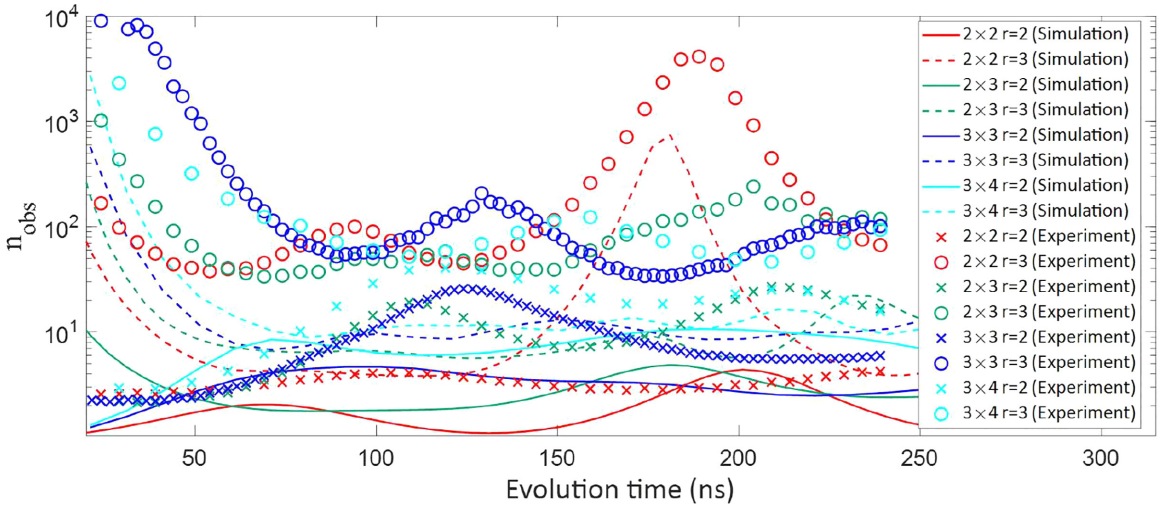

FIG. 11. The expectation of Maxwell's demon observation rounds n_{obs} required for a single trigger of QB in various system size, which are the simulated and experimental values of the second and third rounds respectively.

is $t_{\text{FBtot}} = t_{\text{wait}} + t_r + t_{\text{FB}}$ where t_{wait} is the waiting time to eliminate the AC stark effect after readout, t_r is the readout time, and t_{FB} is the hardware feedback time including readout signal transmission, FPGA demodulation, waveform generation, etc. In typical systems such as [82–84], t_{FBtot} is estimated to be about 10^2 ns, while for the second round, the time caused by feedback is $n_{\text{obs}}(2,t)t_{\text{FBtot}}$ which is approximately several microseconds; at the third round, Maxwell's demon should observe $n_{\text{obs}}(3,t)n_{\text{obs}}(2,t)$ times, so the time caused by feedback is $n_{\text{obs}}(3,t)n_{\text{obs}}(2,t)t_{\text{FBtot}} \sim 10^2\mu$s. Usually the circuit running time needs to be less than one-fifth of the qubit decoherence time to make the experiment valid, so the use of feedback control directly without postselection to observe the demonic effect requires qubit decoherence time around several milliseconds, which are hard to achieve for NISQ processors under current technique.

Now our postselection method reduces the number of feedback operations required by increasing the number of measurements, thereby reducing the circuit duration. In the future, we can mix feedback and postselection method together to optimize the circuit and number of measurements according to the decoherence time of qubit.

5. Background calibration

Before performing our Maxwell's demon experiment, a background calibration experiment is also required due to the fact that our experimental data presented in Fig. 3 are processed using a subsystem conservation postselection method. To verify the remaining data are definitely driven by Maxwell's demon, we measured the background data in the case of two-particle excitation when the iSWAP gate is closed. Similarly, we use the same method to postselect the data, noting that ideally the postselection number of this background would be 0. In reality, it is not 0 due to factors such as thermal excitations, readout errors, Pauli control errors on the iSWAP gate, and of course decoherence. For the double-excitation case, Maxwell's demon acts on the second and third readouts. If our experiment is valid, that is, the events after subsystem conservation postselection method are mainly driven by feedback control of Maxwell's demon, we should see an obvious difference of the postselection rates when the iSWAP gate is ON (experiment) and OFF (background).

So we measured the background of the 2×2, 2×3, 3×3, and 3×4 systems under the double-excitation situation in subsystem B without feedback control (the iSWAP gate is always closed). According to the comparison of each value: red square with red dashed line (blocked), green square with green dashed line, light blue square with light blue dashed line, and the dark blue square with the dark blue dashed line in Figs. 12(a) and 12(b), it is observed that the postselection rate of the system when the iSWAP gate is opened is significantly higher than the background case when the iSWAP gate is closed. We also see that the postselection rate when the iSWAP gate is open is oscillatory in evolution time. This ensures the validity of the subsystem conservation postselection method in this experimental system.

Next it is important to mention that the number of measurement is adjusted according to the system size to ensure that the number of postselection results is sufficient high to ensure the data's statistical significance. The postselection rate SR and the total number of measurements n need to satisfy $\sqrt{P1(i,t,r)[1-P1(i,t,r)]/(SR_n)} < 0.1$ where $P1(i,t,r)$ is defined as the probability of the measurement when the ith qubit is $|1\rangle$ in the rth round of readout at t time. Until all the above processes are completed, we can perform Maxwell's demon experiments by running the circuit of Fig. 5(b).

APPENDIX C: PROCESSING FLOW OF EXPERIMENTAL DATA

To begin, Fig. 13 presents a flow chart of how the experimental data is processed. The experimental data are mainly composed of measurement results in N packets where $N$is typically in the range 10^5–10^6. The data of a complete measurement contain three parts: the measurement condition (including system initial excitation qubits, qubits sequence) represented as a string; the main variable part (evolution time

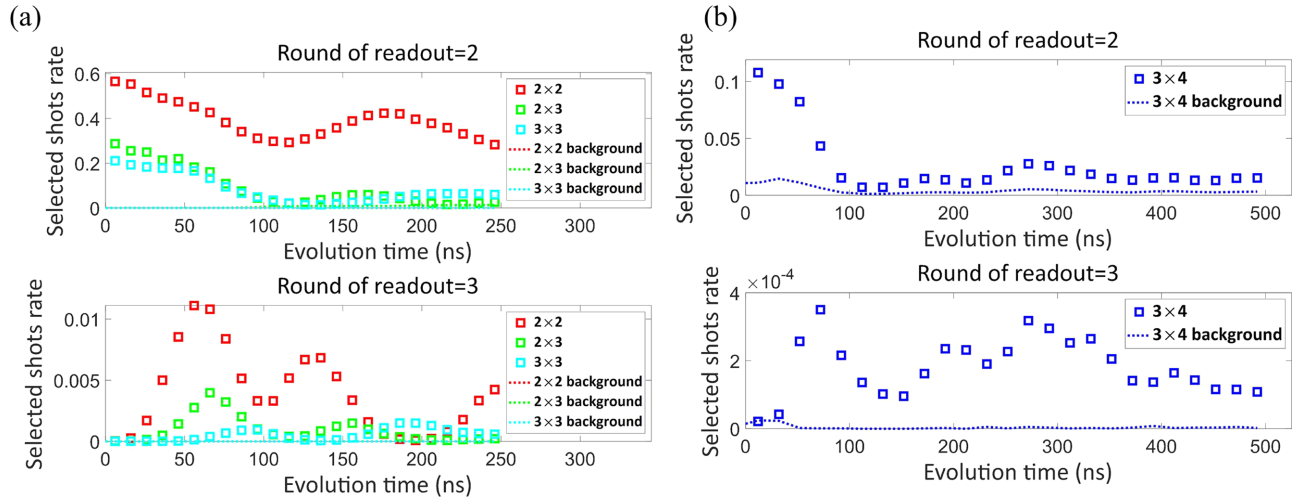

FIG. 12. Postselection rate in first and second readouts of Maxwell's demon QB and background in the double excitation case, and the postselection rate is the ratio of postselection number to the total number of experimental measurements. (a) The number of measurements in the double excitation background experiment is 500 000 for system 2×2, 2×3, and 3×3 respectively. The initial excitation qubits of system 2×2 are "U31Q0" and "U21Q3," while initial excitation qubits in system 2×3 and 3×3 are "U30Q1" and "U21Q3." (b) In system 3×4, the number of experimental measurements and the number of background measurements are both 3 million, and the initial excitation qubits are "U30Q2" and "U21Q3."

t_{evol}, t_{swap}, t_{wait} and other circuit parameters represented as integers; and finally the measurement results of the corresponding qubits at the corresponding moment after each round of readout (Boolean) and all the results of the qubit measurements arranged in order to form the 01 sequence. For the initial single-qubit excitation experiment, each measurement datum contains two sets of the 01 sequence, while for the double-qubit excitation experiments, each measurement contains three sets of readout 01 strings.

First, a Python program decodes the 01-string sequence by decimal code and stores it on the local computer. We then use a Matlab data-parsing program to decode the experimental data by qubit sequence and sort them according to the qubit order. After decoding, the quantum state 01-string data are sorted by each round, corresponding evolution time, number of measurements, and corresponding qubits to obtain a four-dimensional matrix. According to this a four-dimensional matrix, the quantum states of any qubit at any number of rounds, any number of measurements, and any evolution time can be queried for later selection operation and calculation of various physical quantities.

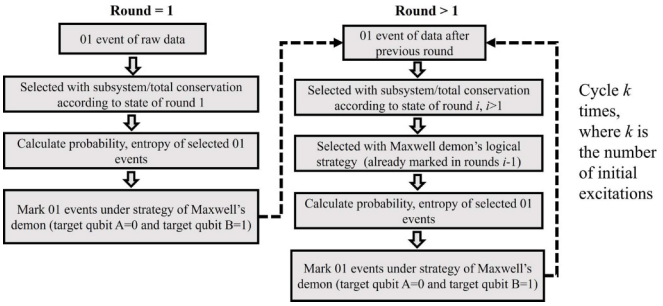

FIG. 13. Experimental data processing flow chart. In the main text, the step of sub-/total system excitation number conservation postselected is used only in the experiment of Figs. 2 and 3.

For the four-dimensional matrix composed of raw data, there are two processing methods: total system conservation and subsystem conservation. The rule of total system conservation is to discard any measurement results whose number of 1 appearing in the 01 string is not equal to the initial number of excitations. This processing rule is applicable to study the working process of Maxwell's demon-type QB in isolated systems. Next for the rule of subsystem conservation, the 01 string is first divided into two corresponding groups by subsystem A/B, and the measurements are discarded when the result of the 01 string in the packet is that the number of 1's appearing in group A is not equal to the theoretical result (increasing sequentially with the number of measurement rounds from 0) or the number of 1's appearing in group B is not equal to the theoretical corresponding result (decreasing sequentially with the number of measurement rounds from the initial excitation number). This processing rule excludes more errors and is applicable to the study of Maxwell's demon selection events as the subject.

To calculate the entropy, we count the subsystem events after postselection to obtain the frequency of each event from which we calculate the probability of the event based on the frequency. We can then calculate various indicators such as the KL divergence, Kryrov complexity (with approximate estimation method), Kolmogorov-Sinai entropy, etc.

1. Timing alignment of horizontal coordinates

The multiqubit evolution of qubits in an experiment requires consideration of the timing alignment. Due to the nonideal nature of the experimental hardware, the timing error consists of three main components:

(i) The XY waveforms may act at different times when multiple qubits are excited simultaneously. For instance,

during a double-excited qubit experiment, if an excited qubit is biased to a predetermined frequency operating point, while another excitation pulse has not arrived yet, it will lead to an experimental error. The waveform delay generated by this error is t_x.

(ii) The actual XY generated by the arbitrary waveform generator for the excited qubit pulses and Z pulses for bias qubits generated by the actual arbitrary waveform generator are not sufficiently accurate, which includes interchannel delays of t_{xz}.

(iii) Z pulse rising edge action time t_z.

Now, if the duration of the detuned waveform used in experiment is t_e, and the transverse time is defined as the evolution time of multiqubit dynamics at the initial moment when all qubits are biased to the predetermined frequency operating point, then the actual transverse coordinate should be $t = t_e - t_x - t_{xz} - t_z$.

2. Errorbar calculation of the probability through σ_z measurement for a single qubit

Each physical quantity involved in the experiment is obtained according to the POVM projection measurement based on probability. Next, we select three physically relevant quantities, namely, the single-qubit measurement probability, the system Shannon entropy, and the multiqubit effective temperature, to illustrate the calculation process for the errorbar.

According to the error transfer equation, the relationship between the standard deviation of entropy and the probability in the rth round of the readout at time t is

$$S_{\mathrm{err}}(t,r) = \sqrt{\sum_i P1_{\mathrm{err}}(i,t,r)^2 \left\{ \log_2[P1_{\mathrm{err}}(i,t,r)] + \frac{1}{\ln 2} \right\}}, \tag{C1}$$

where $P1_{\mathrm{err}}(i,t,r)$ is the statistical standard deviation of the measurement of $|1\rangle$ for the ith qubit in the rth round of readout at time t. Since the result the quantum state measurement is either 0 or 1 for a two-point distribution, the probability standard deviation for the n repetitive sampling case at time t for the multiqubit evolution is

$$P_{\mathrm{err}}(i,t,r) = \sqrt{P1(i,t,r)[1 - P1(i,t,r)]/n}. \tag{C2}$$

3. Errorbar calculation of the multiqubit Shannon entropy

After considering postselection, the sampling number is the actual number of valid measurements $s(t,r)$ at time t for the rth round of readout. Combining Eqs. (C1) and (C2) yields the standard deviation of the multiqubit evolution time t entropy at the rth round of readout as

$$S_{\mathrm{err}}(t,r) = \sqrt{\sum_i \left\{ \frac{P1(i,t,r)[1 - P1(i,t,r)}{s(i,t,r)} \right\} \left\{ \log_2 \sqrt{\frac{P1(i,t,r)[1 - P1(i,t,r)]}{s(t,r)}} + \frac{1}{\ln 2} \right\}}.$$

4. Errorbar calculation of the temperature for multiqubit system

First, when considering a spin half particle (jth qubit) in a thermal field, the jth mean photon number is given by

$$n_j = \frac{1}{e^{\frac{\hbar\omega_j}{kT_j}} + 1} \quad \begin{array}{l} \to 0 \quad (\text{when} \quad T_j \to 0) \\ \to 1/2 \quad (\text{when} \quad T_j \to \infty). \end{array} \tag{C3}$$

Now for an ensemble of N qubits, we can determine the average photon number n_{ave} as

$$n_{\mathrm{ave}} = \left(\sum_j n_j \right) \Big/ N. \tag{C4}$$

So we can determine n_{ave} and T_{ave} through

$$n_{\mathrm{ave}} = \frac{1}{e^{\frac{\hbar\omega_j}{kT_{\mathrm{ave}}}} + 1}. \tag{C5}$$

This is the average quantity across all qubits in that part of the ensemble. Hence we can determine the "effective temperature" of the ensemble in many-qubits system.

Next, according to the error transfer equation, the relationship between the standard deviation of the effective temperature of the multiqubit system in the rth round of readout at time t and the standard deviation of the system's probability is

$$T_{\mathrm{err}}(t,r) = \frac{\partial T_{\mathrm{eff}}}{\partial n_{\mathrm{ave}}} n_{\mathrm{err,ens}}(t,r) = \frac{\partial T_{\mathrm{eff}}}{\partial P} P_{\mathrm{err}}(i,t,r). \tag{C6}$$

We can calculate the error bar $n_{\mathrm{err,ens}}$ of the ensemble with N qubits using $\sum_{j=1}^{N} \frac{\partial n_{\mathrm{err,ens}}}{\partial n_{\mathrm{err,j}}} = \mathrm{mean}[n_{\mathrm{err,j}}(i,t,r)]$, where $\mathrm{mean}[n_{\mathrm{err,j}}(i,t,r)]$ is the statistical mean of the errorbar of all single qubits n_j.

We could calculate the errorbar of the work, $\langle W \rangle / k_B T$, and other physical quantities based on the errorbar of the probability and the effective temperature. The data processing process has shown in Fig. 13.

APPENDIX D: SIMULATION AND OPTIMIZATION METHOD

The Hamiltonian of our system can be described by Bose-Hubbard model [32,85,86] as

$$\hat{H} = \sum_{j \in \{Q_i\}} \hbar\omega_j \hat{a}_j^\dagger \hat{a}_j + \frac{\hbar U_j}{2} \hat{n}_j (\hat{n}_j - 1) + \sum_{j \in \{Q_i\}, i \in \{C_{Q_i}\}} \hbar J_{\mathrm{eff}}^{i,j} (\hat{a}_i^\dagger \hat{a}_j + \hat{a}_i \hat{a}_j^\dagger), \tag{D1}$$

where $\hat{a}_j^\dagger$ and $\hat{a}_j$ are the usual creation and annihilation operators of the hard-core boson corresponding to the jth qubit, $\omega_j/2\pi$ is the frequency of the first energy gap in the jth qubit, U_j is the anharmonicity of qubit, $J_{\text{eff}}^{i,j}$ is the effective coupling strength between $\mathrm{Q_i}$ and $\mathrm{Q_j}$ through the resonant cavity, while $\{C_{\mathrm{Q_i}}\}$ denotes the set of qubits coupled to $\mathrm{Q_i}$. The system is composed of transmons that satisfy $\mathrm{U/J} \gg 1$ meaning the hard-core Bose-Hubbard model is equivalent to the XX spin model [86–88]. When all qubits are aligned to the same frequency, the Hamiltonian has the form

$$\hat{H}_{\text{evo}} = \sum_{i\in\{Q_i\}, j\in\{C_{Q_i}\}} \hbar J_{\text{eff}}^{i,j}(\hat{a}_i^\dagger \hat{a}_j + \hat{a}_i \hat{a}_j^\dagger). \tag{D2}$$

For the Maxwell's demon experiment using a quantum many-body system, we simulate it in the following way:

(1) *Simulation of the evolution process.* The Schrödinger equation can be represented in the form

$$|\Phi(t)\rangle = e^{-iHt/\hbar}|\Phi(0)\rangle, \tag{D3}$$

where $|\Phi(0)\rangle$ is our the initial state while $|\Phi(t)\rangle$ is the state of system at time t. We numerically simulate the state of the system at time t using the Hamiltonian matrix and the initial state.

(2) *Simulation of multiple rounds of measurements.* For a given evolution time t_{evol}, the quantum state of the system is $|\Phi(t_{\text{evol}})\rangle$ from which the probability distribution $P(t_{\text{evol}}) = |\Phi(t_{\text{evol}})|^2$ can be determined. By sampling according to this probability distribution, the measurement results can be simulated.

(3) *Maxwell demon's swap operation.* The quantum states obtained by sampling in step 2 are exchanged as the excitation of the two qubits $target_A = |0\rangle$ and $target_B = |1\rangle$ as the Maxwell's demon feedback control. These are then used as the initial states for the next round of evolution.

(4) *Postselection.* The measured simulation results in step 2 are selected to satisfy the Maxwell's demon condition $target_A = |0\rangle$ and $target_B = |1\rangle$.

(5) *System synthesis simulation.* We repeat the sampling simulation N times to determine the results of the N event experiment.

1. Disorder optimization

Our numerical simulations use a Hamiltonian learning method to solve them. However, the frequencies of the different qubits cannot be perfectly aligned, meaning there is a certain amount of disorder among those frequencies. We set the initial disorder matrix as the finalized values for the disorder measured after frequency aligned. We start from it, and reduce the distance between the simulated value and the experimental value with the global random search algorithm and the local Nelder-Mead. We then use the Shannon entropy to compare the experiment and simulation results.

2. Shannon entropy

Figures 14(a)–14(h) present the experimental data and simulation results for the evolution of Shannon entropy with time for the various system sizes 2×2, 2×3, 3×3, 3×4 respectively. According to the results our 2×2 system is equivalent to a cyclic 1D chain where the entropy $S_r(t)$ measured in each round oscillates with t_{evol} spontaneously. This makes it difficult to be properly thermalized. The structure of the 3×4 system is 2D array, and as we observe the oscillation of $S_r(t)$ is obviously smaller when $t_{\text{evol}} > 50$ ns. Comparing the individual plots, it can be easily observed that the fluctuation of $S_r(t)$ relative to the maximum entropy $S_{r,\max}$ is significantly lower for the 3×4 system than the 2×2 system. Also, in both systems $\mathrm{std}[S_2(t)] < \mathrm{std}[S_1(t)]$. In system 2×2, the maximum value of $S_r(t)$ can still reach $S_{r,\max}$, while system 3×4 is thermalized at $t_{\text{evol}} > 50$ ns and its $S_r(t)$ converges to $S_{r,\max}$. Comparing the different dynamical characteristics between the two systems, it can be seen that the oscillation amplitude of information entropy in the system with small size effect is higher than larger size. Further we observe that the rise and fall of the Shannon entropy relative to the maximum entropy generally decreases as the size of the system increases. Meanwhile, the increase and decrease of Shannon entropy at $r = 2$ is significantly lower than the increase and decrease of Shannon entropy at $r = 1$.

In the ideal situation, if all qubits' frequencies and the coupling strength between all neighbor qubits are completely equal, the system reaches the thermalized microcanonical ensemble. Then all eigenvalues when we diagonalize the Hamiltonian are the same, while all eigenvectors are calculated with equal probability, which corresponds to the maxium frequency in Fig. 14.

3. KL divergence related to microcanonical ensembles

We can also calculate the Kullback-Leibler divergence (KL divergence) of a system with different size to determine the degree of thermalization in realistic experimental conditions.

As shown in Fig. 15, compared to the result of KL divergence in subsystem 3×4, the subsystem 2×2 is obviously far from microcanonical ensembles. Due to the limited number of qubits and realistic experimental conditions (e.g., frequency disorder/the coupling strength between neighboring qubits is not equal, etc.), the KL divergence in subsystem 3×4 is not zero perfectly but around 0.2 when $t_{\text{evol}} > 50$ ns.

APPENDIX E: DYNAMICAL ERGODICITY AND THE PERFORMANCE OF QB

For a 2D hard-core Bose-Hubbard model, a system with a finite-size effect is always periodic, while the system with enough size will evaluate to ETH finally (making the loss of initial state information). In addition to the Shannon entropy, it is helpful to use the dynamical entropy to characterize the system more accurately to describe the spatio-temporal characteristics of the dynamical processes inside the QB.

In our experiments, the kinetics of the Krylov complexity (reflecting the spatial geometric characteristics), the Kolmogorov-Sinai entropy (KSE) (reflecting the time series characteristics), and the Shannon entropy rate (reflecting the thermodynamic characteristics) can be used to characterize the dynamical evolution process of Maxwell's demon-type QB operation.

1. Krylov complexity inside the QB

Our first consideration will be the spatial geometric characteristics of the QB. As a mathematical tool in many-body

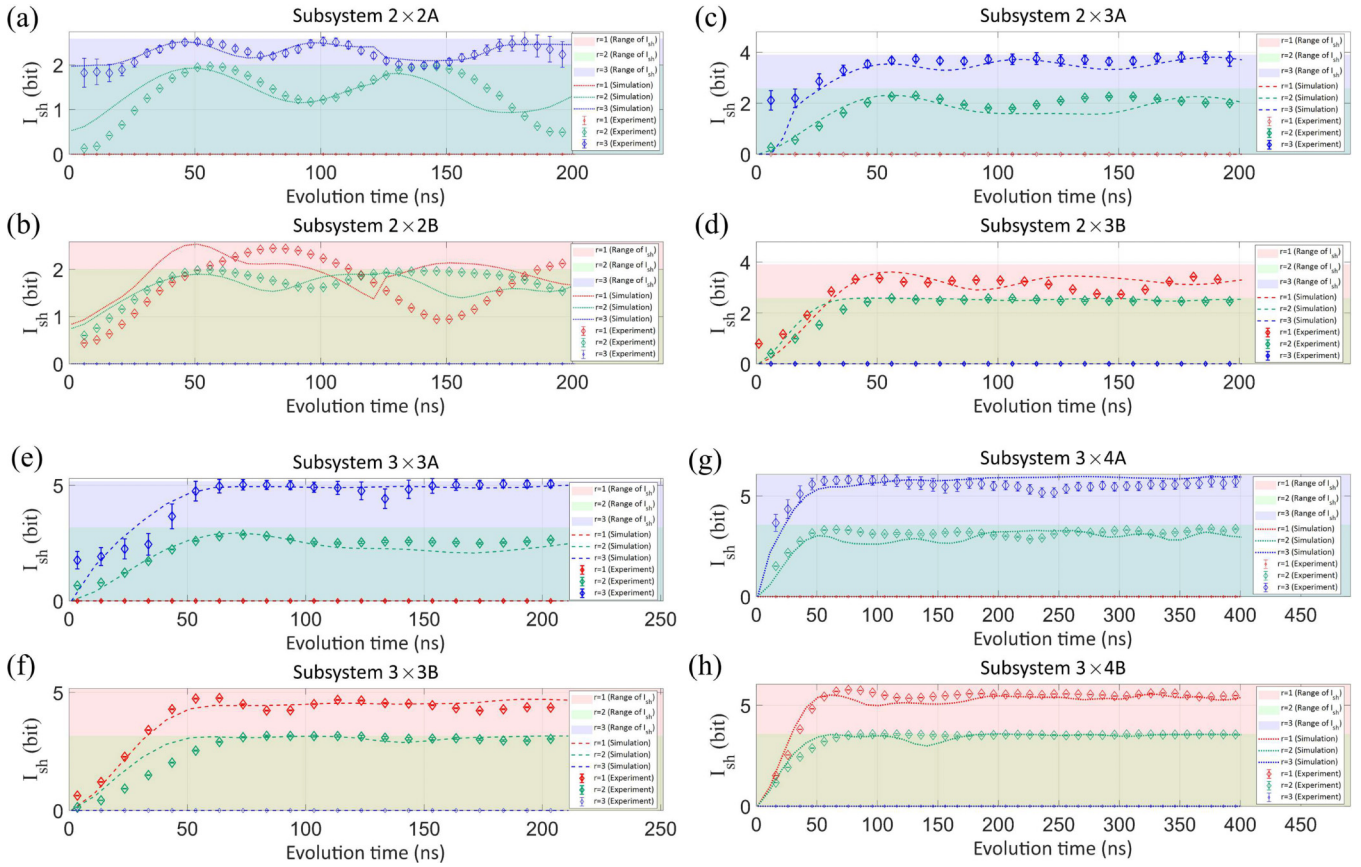

FIG. 14. Exploration of the Shannon entropy in the Maxwell's demon QB. The number of experimental measurements is 1 million for the system sizes 2×2, 2×3, and 3×3 and 3 million for the 3×4 system size. The number of simulation points is 500 000 for the 2×2, 2×3, and 3×3 system sizes and 1 000 000 for the 3×4 case. The initial excitation qubits are "U21Q3" and "U31Q0" in the system 2×2, and "U30Q1" and "U21Q3" for the 2×3 and 3×3 systems. "U30Q2" and "U21Q3" are excited in the 3×4 system. (a)–(h) Simulated and experimental values for Shannon's entropy against the evolution time for the various system sizes. The maximum entropy of system 2×2 is 2 and 2.585 for rounds 1 and 2, respectively, 2.585 and 3.907 for the 2×3 system, and 3.167 and 5.170 for the 3×3 system. Maximum entropy of the 3×4 system is 3.585 and 6.044 for rounds 1 and 2, respectively. The red, green, and blue background marks the theoretical upper bounds of maximum entropy for three rounds, respectively, while the red, green, and blue data diamond points in each graph present the entropy at $r = 1$, $r = 2$, and $r = 3$, respectively. The dashed lines of the same color are corresponding simulation values.

quantum dynamics, Krylov complexity [49,50] can reflect the effect of geometric structure of quantum system on phase space dynamics. First, based on the geometric structure of system, the phase space states are divided into a set of complete Krylov bases $\hat{K} = \{|\xi(0)\rangle, |\xi(1)\rangle, |\xi(2)\rangle, \ldots, |\xi(n)\rangle\}$, where i is the Krylov coefficient and $|\xi(0)\rangle$ the initial state (for the initial state event the Krylov coefficient is 0).

The Krylov coefficient is usually determined through the Lanczos recurrence method. Further for the scar state or Sachdev-Ye-Kitaev (SYK) model, the Krylov coefficient can be solved accurately [89]; however, for Bose-Hubbard models, its tedious to calculate the Krylov coefficient accurately. Here we created a pragmatic way to estimate Krylov coefficients instead of using the Lanczos algorithm. Since most of the coupling strengths between two qubits in subsystem A are in the 2.3–2.5 MHz range, the qubit states' propagation time to the proximity qubits is approximately equal. As such we set δt as the time required to propagate a qubit state to another adjacent qubit with the Hamiltonian $H(\delta t)$. For the state vector $|\xi(t)\rangle$ under the action of

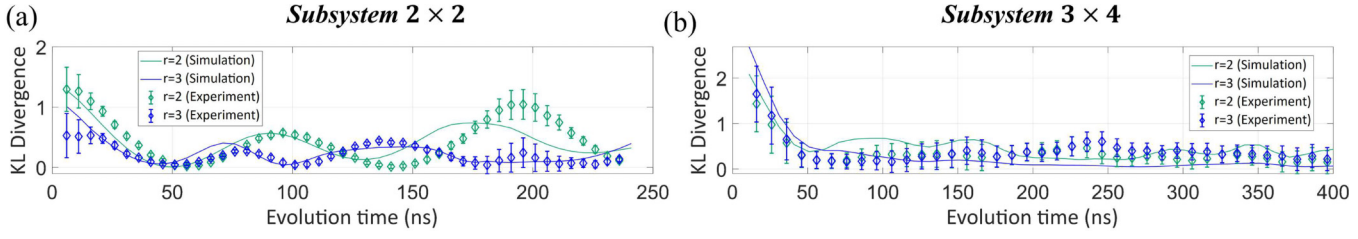

FIG. 15. KL divergence of system 2×2 and system 3×4 related to microcanonical ensembles.

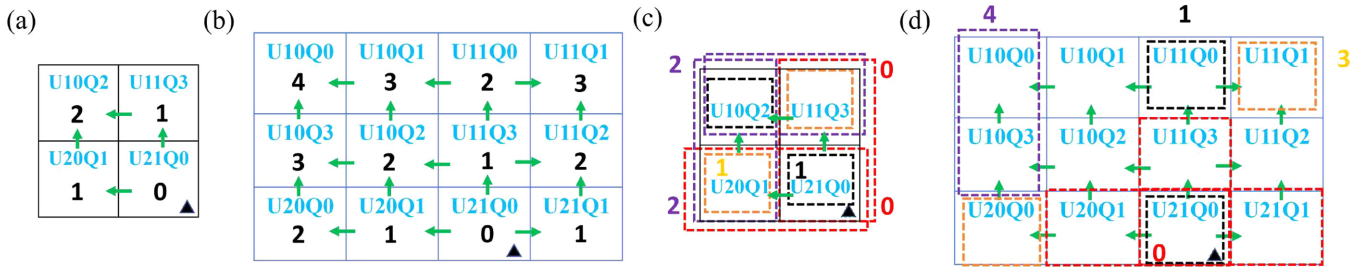

FIG. 16. Approximate estimation algorithm of Krylov coefficients in our QB. The target qubits are identified by black triangles. (a) Derivation of Krylov coefficients for the system 2×2 under single excitation where the green arrow shows the direction of state propagation, while the black numbers are the Krylov coefficients. (b) Krylov coefficients for the single excited 3×4 system 3×4. (c) Krylov coefficients for the 2×2 system under double excitation. The different events are surrounded by dashed boxes of different colors (six total), while their Krylov coefficients are marked with corresponding colors. (d) The Krylov coefficients for the doubly excited 3×4 system. There are 66 different kinds of basic events under the particle number representation. The events enclosed by red dashed boxes are the initial states, and there are three kinds of events: Krylov coefficient of the events enclosed by black dashed boxes contain target qubit A, which is 1; Krylov coefficients of the events enclosed by orange dashed boxes, which is 3; and Krylov coefficients of the events enclosed by purple dashed boxes, which is 4.

Hamiltonian time-containing evolution operator as $|\xi(t)\rangle = |\xi(0)\rangle e^{-i\hat{H}t/\hbar}$, and dividing t uniformly into the sum of n δt, then we have $e^{-i\hat{H}t/\hbar} = e^{-i\hat{H}\sum_{i\to n}\delta t} = \prod_{i\to n} e^{-i\hat{H}\delta t/\hbar}$ with $|\xi(t+\delta t)\rangle = |\xi(t)\rangle e^{-i\hat{H}\delta t/\hbar}$.

With Markov condition, the Krylov coefficient is the minimum number of steps required to generate the state A from our initial state. We define this as min(spread(A), spread(A)) which is the number of steps for the propagation of the A event from the initial event. There are different ways to divide the set of phase space measures μ. Under particle number representation, the fundamental events constituted by the dynamical evolution of n qubits and k initial excitations can be divided into C_n^k events. For example, when the number of excitations is 1, the phase space is partitioned into the set of measures consisting of the basis vectors $|\xi\rangle \in \{|100\cdots000\rangle, |010\cdots000\rangle, \ldots, |000\cdots001\rangle\}$. According to Fig. 16, quantum states always propagate from low Krylov coefficients to high Krylov coefficients. For multiple excitations, there is more than one initial state event and propagation path, and so the shortest propagation path number for the longer qubit is chosen as the Krylov coefficient; that is, $K(AB) = \max\{\min[\text{spread}(A)], \min[\text{spread}(B)]\}$. Since the initial state of target qubit A(U21Q0) in the system of Maxwell's demon operation A is necessarily $|1\rangle$, then the number of propagation of events containing target qubit A is processed minus 1. That is, we have K(AB) = max{min[spread(A)],min[spread(B)]} for target$A \notin A \cup B$ and K(AB) = max{min[spread(A)],min[spread(B)]}-1 for target$A \in A \cup B$. We can write the Krylov complexity as

$$Kc(t) = \sum_{A,B\in\Omega(C_n^k)} K(AB)P[|\xi_{AB}(t)\rangle], \tag{E1}$$

where $\Omega(C_n^k)$ is the set of states constituted by the dynamical evolution of the system with k initial excitations in n qubits under the particle number representation. The experimental data are filtered in a subsystem conservation manner, which ensures the completeness of the data set in the measure space.

2. Kolmogorov-Sinai entropy inside the QB

Our second investigation will be the time series analysis inside the QB. Pesin's theorem [90–92] pointed out that KSE is the sum of positive Lyapunov exponents, which can characterize chaotic dynamics of the system adequately. So a higher KSE will lead to a system with more instability. In large systems the dynamical process are often divided into two phases [51], the prethermalized phase with unstable dynamics trajectory, which still preserve information of initial state. When KSE decays to 0, the system reaches ETH, and the dynamics trajectory fills the phase space, which will no longer change. According to the definition $E_{\text{KS}}(T) = sup_{|\xi(t)\rangle} h_\mu[T, |\xi(t)\rangle]$, where μ is the division of phase space measure set and *sup* is the upper exact bound, for a dynamical trajectory during time T, KSE [93] is

$$E_{\text{KS}} = -\lim_{T\to\infty} \sum_{hist\ 0\to T} \frac{\sum_{his(t)\ 0\to T} P[|\xi_r(t)\rangle]\ln[|\xi_r(t)\rangle]}{T\sum_{his(t)\ 0\to T} P[|\xi_r(t)\rangle]} \tag{E2}$$

with *hist* being short for *historics*. According to the completeness condition in the measure space $\sum_{his\ 0\to T} P[|\xi_r(t)\rangle] = 1$ with Markov condition, we have

$$E_{\text{KS}} = -\frac{1}{\delta t} \sum_{\xi,\xi'\in V_\mu} P[|\xi_r(t)\rangle]w(\xi\to\xi')\ln\, w(\xi\to\xi'), \tag{E3}$$

where V_μ is the set of all measured events when the phase space is divided in the way of μ, $w(\xi\to\xi')$ is the probability when the system transforms from ξ to ξ' after δt, and the corresponding case when the phase space of the system does not change is $w(\xi\to\xi) = 1 - w(\xi\to\xi')$. Then the phase space dynamics trajectory dispersion rate $E_{\text{KS}}(r)$ of Maxwell's demon experiment for the rth round with sampling period fixed at δt is

$$\begin{aligned} E_{\text{KS}} &= \frac{1}{\delta t}\sum_{\xi\in V_\mu} P[|\xi_r(t)\rangle][1-w(\xi\to\xi)]\ln[1-w(\xi\to\xi)] \\ &= -\frac{1}{\delta t}\sum_{\xi\in V_\mu} P[|\xi_r(t)\rangle]\{1-P[|\xi_r(t)\rangle]P[|\xi_r(t+\delta t)\rangle]\} \\ &\quad\times \ln[1-P[|\xi_r(t)\rangle]P[|\xi_r(t+\delta t)\rangle]], \end{aligned} \tag{E4}$$

where $P[|\xi_r(t)\rangle]P[|\xi_r(t+\delta t)\rangle]$ is the probability that the phase space trajectory remains constant after the sampling interval δt.

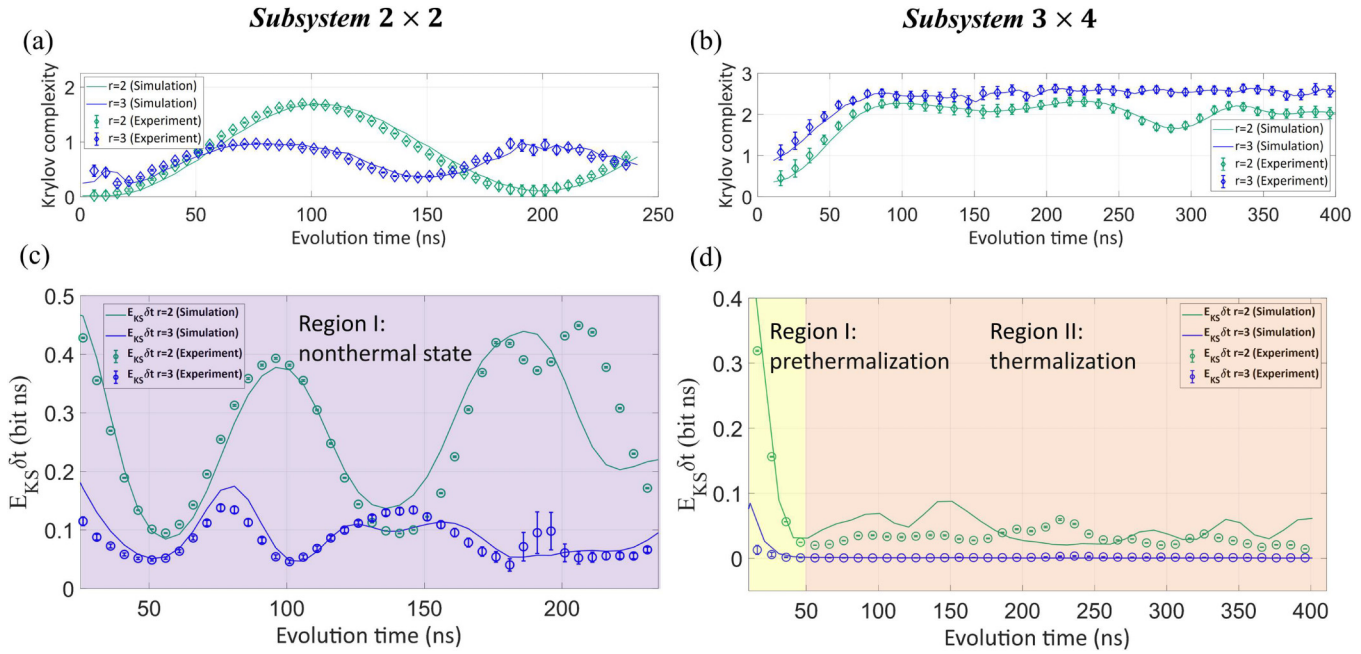

FIG. 17. Dynamics of ergodicity indicator in our QB where the number of experimental measurements is 1 million (3 million) for the 2×2 (3×4) system respectively. The number of simulation points is 0.5 million (1 million) for the 2×2 (3×4) systems. (a) Dynamics of the Krylov complexity for the 2×2 subsystem A. (b) Dynamics of Krylov complexity for the 3×4 subsystem A. (c) $E_{\mathrm{KS}}\delta t$ in the 2×2 subsystem A, where the system is in a nonthermal state (marked with purple color). (d) $E_{\mathrm{KS}}\delta t$ in the 3×4 subsystem A, where the system evolves in two stages: the prethermalized phase (yellow) and the thermalized phase (light orange).

Moreover, the integrability of quantum systems is also closely related to the system size and geometric topology [94–97], which will be an intriguing question for us in the future.

3. Store work utilization in phase space and the reconstruction of Shannon entropy

The energy of multiqubit QB could be divided into two parts: the work which has the potential to extract and the residual energy. It is known [42] that the maximum work that can be extracted from a thermodynamic system with entropy S is the *ergotropy*:

$$W_{Ergotropy} = \sum_{j,k} r_j \epsilon_k (|\langle r_j|\epsilon_k\rangle|^2 - \delta_{jk}). \tag{E5}$$

In the quantum version, the *ergotropy* is the maximum value in all range of extracted work as

$$W_{Ergotropy} = \max\{\mathrm{Tr}\{H[\rho(t) - \sum_{m\in i,j} E_m|m\rangle\langle m|]\}\}, \tag{E6}$$

where $\rho(t)$ is the density matrix of dynamical evolution for the system, which is related to the quantum system's ergodicity. Therefore, there is $W_{Ergotropy} \geqslant \mathrm{Tr}[H(\rho(t) - \sum_{m\in i,j} E_m|m\rangle\langle m|)] \geqslant 0$.

Now the utilization of the maximum extracted work is given by

$$\eta(t) = \frac{\mathrm{Tr}\{H[\rho(t) - \sum_{m\in i,j} E_m|m\rangle\langle m|]\}}{W_{Ergotropy}}. \tag{E7}$$

Since the microscopic state number of the system in phase space is closely related to the efficiency of *ergotropy* inside the QB. Then we can reconstruct its microscopic state information through large number of repetitive projection measurements before and after the feedback loop of Maxwell's demon. Then, with reference to the maximum phase space, the stored work rate occupied in phase space before and after the action of Maxwell's demon's rth feedback control under the two-point measurement protocol could be defined as

$$\eta_{\mathrm{e}}(t) = \frac{\Omega_r(t) - \Omega_{r-1,\max}}{\Omega_{r,\max} - \Omega_{r-1,\max}}, \tag{E8}$$

where $\Omega_r(t)$ is the evolution of desirable microscopic state basis vector with dynamics of the quantum system in Hilbert space under the particle excitation number representation. For the n-qubit system with k excitation numbers, its desirable microscopic state basis vector is $\Omega(n,k) = C_n^k$, and its Shannon entropy of the maxium phase space is calculated as $\log_2 C_n^k$ according to the principle of equal probability. Accordingly the stored work rate occupied in phase space mapping to the space of Shannon entropy can be defined as

$$\eta_{\mathrm{Sh}}(t) = \frac{S_r(t) - S_{r-1,\max}}{S_{r,\max} - S_{r-1,\max}}. \tag{E9}$$

4. Dynamical ergodicity in experiment

Let us now show the results of dynamical ergodicity which could highly affecting the performance of multibody QB, Kryrov complexity, and KSE in our experiments. As shown in Figs. 17(a) and 17(b), the Kryrov complexity of system with finite-size effect varies periodically with period of 188 ns in the second round and 124.7 ns in the third round. Meanwhile the dynamics of system 3×4 is clearly divided into two regions: a prethermalized state (for $t_{\mathrm{evol}} < 50$ ns) and

a thermalized state (for $t_{\text{evol}} > 50$ ns). The Kryrov subspace complexity in the prethermalized state grows exponentially with time t, and we can calculate the change rate of KS entropy $E_{\text{KS}}\delta t$ when the sampling interval $\delta t = 5$ ns.

Though Figs. 17(c) and 17(d), we can observe that the $E_{\text{KS}}\delta t$ of 2×2 system with finite size effect is always unstable with t_{evol} in each round. For the larger system, $E_{\text{KS}}\delta t$ decays rapidly in the prethermalized state and tends to 0 in the thermalized state. Both systems have $E_{\text{KS}}\delta t$ in the third round smaller than second round.

APPENDIX F: TPM PROTOCOL OF TWO-LEVEL SYSTEMS AND QUANTUM MEASUREMENT BACKACTION

1. The TPM protocol

In this experiment, in order to calculate the change of thermodynamic quantity for two-level system during the evolution process, the σ_z projective measurement of the two-level system before and after the operator U is projected and measured successively. Then the results of the two measurements are used to calculate the variation of thermodynamic quantity, which are named the *two-point measurement* (TPM) protocol:

$$U^{\dagger}HU - H. \tag{F1}$$

Considering a two-level system with energy eigenstates $|i\rangle$, $|j\rangle$, its Hamiltonian could be written as $H = \sum_{m\in i,j} E_m|m\rangle\langle m|$. The energy eigenvalues of the two-level system are E_i and E_j, then the average of the mechanical quantities of the operator U is $\langle i|U|i\rangle$, and the conditional probability of the system changing from $|i\rangle$ to $|j\rangle$ by the action of the U operator is $p_{i\to j} = |\langle i|U|j\rangle|^2$.

Now the conditional probability that system works as W via the U operator under the TPM protocol is

$$p(W) = \sum_{m\in i,j} \delta(W - W_{i\to j})p_{i\to j},$$

where $W_{i\to j} = E_j - E_i$, $p(W) = \sum_{m\in i,j}\delta[W - (E_j - E_i)]p_{i\to j}$ where δ is the Dirac delta function. The mean value of the work of the system acting via the U operator is $\langle W\rangle = tr[\sum_{m\in i,j} p(W)E_m|m\rangle\langle m|]$.

It is worth noting that the TPM protocol still has limitations. Reference [56] pointed out that when we make two projection measurements for a certain quantum thermodynamical observation, the statistical information of the second measurement will be deformed since the quantum projection measurement destroys the quantum superposition of system. Without violating the fundamental fluctuation theory of quantum thermodynamics, the distortion cannot be completely eliminated, but the effect can be reduced by means of collective measurements.

2. Quantum measurement backaction

The interaction during quantum measurements [37] contains a amount of fascinating physics that warrants further discussion. Therefore, the quantum measurement process in our experiment will lead to a "violation" of the Sagawa-Ueda equality because the whole system is no longer excitation number conserved under the destructive nature of quantum measurement. Based on the above facts, let us further analyze the measurement backaction of the experimental process.

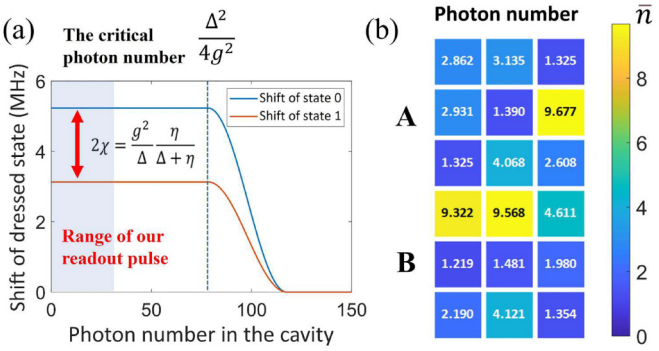

FIG. 18. (a) Photon number vs the dispersive shift of the dressed cavity for target qubit B (U21Q3), where χ can be calculated by the coupling strength between the qubit and the resonator g, the frequency difference of qubit and the resonator $\Delta = |\omega_q - \omega_r|$, and the anharmonicity η. (b) The photon number $\bar{n}$ of every qubit used in the experiment.

The measurement process of the qubit in our experiment can be regarded as an indirect measurement of the cavity coupled to the qubit. The coupling of the qubit and the cavity makes the frequency of the cavity different for the qubit in either the 0 state or the 1 state, and then the measuring process is manifested as in the frequency shift of the dressed cavity as shown in Fig. 18. Thus, the effect of the measurement operator will cause the frequency shift of this dressed state; e.g., a dispersive measurement will lead to an energy increase in the dressed state $\Delta E_{QM} = E_{*,1} - E_{*,0}$, where $E_{*,0}$, $E_{*,0}$ are the two energy levels of the dressed state when the qubit is $|1\rangle$ or $|0\rangle$, respectively.

However, although the readout pulse is mostly absorbed by the dressed cavity, the number of photons in the cavity still has an effect on the qubit. So, in our setup, the involvement of measurements in the process is manifested as the Stark effect [98]: $\Delta_{Starkshift} = 2\frac{\kappa^2}{\kappa^2+4\chi^2}\chi\bar{n}$

So the energetic effects due to the measurement backaction can be calculated through the number of photons in the dressed state and the parameters presented in Fig. 6.

APPENDIX G: MUTUAL INFORMATION AND THE GENERAL JARZYNSKI RELATIONS UNDER THE TPM PROTOCOL

1. Discussion of qubit-environment interaction

In Fig. 4 we varied the readout pulse amplitude of target qubit B to obtain different measurement error sequences. The length of readout pulse was 500 ns. The standard readout amplitude is optimized according to the hardware, while we adjust the wave amplitude based on the standard readout amplitude. Then we get a sequence varying from 0.05 to 0.75 times the standard amplitude, 15 points in total. Relations between the photon number $\bar{n}$ and the total measure error of target qubit B (U21Q3) are shown in Fig. 18.

As shown in the main text, we observed the violation of the original Sagawa-Ueda equality due to the qubit-environment interaction. Apart from the measurement backaction,

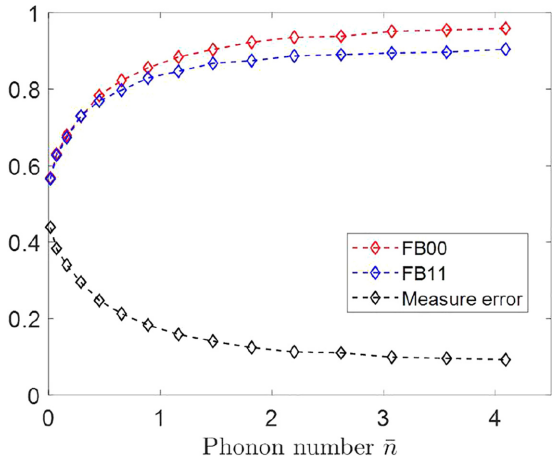

FIG. 19. Relation between the photon number and measurement error of target qubit B (U21Q3).

$|0\rangle \to |1\rangle$ transition is mainly caused by the thermal excitation, while the $|1\rangle \to |0\rangle$ transition is mainly caused by the decoherence. So the two terms could be calculated through

$$E_{thermal} = \sum_i P_i(|1\rangle) e^{-\frac{hf_i}{k_B T_{\text{est,i}}}}, \tag{G1}$$

$$E_{decoherence} = -hf_i \sum_i P_i(|1\rangle)\left(1 - e^{-\frac{t_{\text{circuit}}}{T_{1,i}}}\right), \tag{G2}$$

where $T_{\text{est,i}}$ is the thermal excitation temperature of the ith qubit, t_{circuits} is the circuit time, and $T_{1,i}$ is the decoherence time of the ith qubit.

So the qubit-environment interaction $\hat{H}_{q-env}$ can be calculated through the quantum measurement backaction (Stark shift in our setup), the decoherence, and the thermal excitation.

Meanwhile, the circuit length is 0.811 μs and includes a feedback loop and two measurements. For the rth readout round, the measurement error is $\epsilon(r) = 1 - P_{\text{targetB}}(|0\rangle)F_{\text{targetB0}\to 0}(r) - P_{\text{targetB}}(|1\rangle)F_{\text{targetB1}\to 1}(r)$, where $P_{\text{targetB}}(0, 1)$ is the probability of target qubit B for $|0, 1\rangle$, $F_{\text{targetB0}\to 0}$ is the $|0\rangle$ readout fidelity of target qubit B, and $F_{\text{targetB1}\to 1}$ is the $|1\rangle$ readout fidelity. Relation between the photon number and the measurement error of target qubit B is shown as Fig. 19.

2. Mutual information under the TPM protocol

The mutual information in a single term and total average mutual information are given by $I(nm) = \ln[P(n|m)] - \ln P_{\text{make}n}$, $\langle I\rangle = \sum_{nm} P(nm)I(nm)$ respectively, where nm is the combined event of preparing the n state and measuring the m state, $P(nm)$, $I(nm)$, respectively, for the probability of occurrence of the corresponding event and the mutual information. Next $P(n|m)$ is the conditional probability of the m state measured under the premise of preparing the n state while $P_{\text{make}n}$ is the probability of preparing n states. For a single measurement of target qubits, the mutual information has four terms. While in the generalized Jarzynski relations, the two measurements of the initial and final states correspond to the operation before and after the iSWAP gate, the mutual information has 16 terms (more details later).

a. Mutual information under a single POVM measurement

Here the qubits are prepared to states n and the single quantum mutual information is experimentally measured to be m states as $I(nm) = \ln[P(n|m)] - \ln[P(n)]$. For a single POVM measurement there are four cases of nm, namely, 00, 01, 10, and 11, which can be calculated according to readout fidelity of target qubits. The total mutual information of target qubits is $\sum_{nm} P_{\text{make}n} I(nm)$. For a single qubit, this mutual information is divided into four terms, which are

$$I(00) = \ln(F_{00}) + \ln P_{\text{make0}}, \tag{G3}$$

$$I(01) = \ln(1 - F_{00}) + \ln P_{\text{make0}}, \tag{G4}$$

$$I(10) = \ln(1 - F_{11}) + \ln P_{\text{make1}}, \tag{G5}$$

$$I(11) = \ln(F_{11}) + \ln P_{\text{make1}}, \tag{G6}$$

where F_{00} is the measured probability of the $|0\rangle$, that is, the readout fidelity of $|0\rangle$ conditioned on preparing the $|0\rangle$ accurately. Similarly F_{11} is the $|1\rangle$ readout fidelity, conditioned on preparing the $|1\rangle$ accurately. In our experiment, the measured value of $|1\rangle$ state probability with the measurement error at this time is calculated according to the measurement of $P_{\text{make}n} = \frac{P(|1\rangle)}{\epsilon}$ of the corresponding qubit before Maxwell's demon operation.

The single-qubit measurement mutual information average is summed over the product of each single mutual information and the corresponding probability of event occurrence as follows:

$$\langle I\rangle = \sum_{nm} P(nm)I(nm) \tag{G7}$$

$$= \ln 2 + \epsilon \ln(\epsilon) + (1 - \epsilon)\ln(1 - \epsilon). \tag{G8}$$

b. Mutual information under the TPM protocol of initial and final states

The Sagawa-Ueda equality is the modified Jarzynski equality valid with the presence of Maxwell's demon. Under the TPM protocol, the measurement error is ϵ. Maxwell's demon operates the qubit whose initial state are labeled as i and the final state are labeled as f. If the measurement result for the initial state is i' and final state is f', then the probability of this event [55] is

$$P(fi; f'i') = [(1 - \epsilon)\delta_{ff'} + \epsilon(1 - \delta_{ff'})][(1 - \epsilon)\delta_{ii'} + \epsilon(1 - \delta_{ii'})], \tag{G9}$$

where f, i, f', i' takes the value of either 0 or 1. Then the total number of mutual information between the initial and final states of the qubit is 16, which are

$$I(ff'; ii') = \ln \frac{P(fi; f'i')}{p(i)p(i \to f)}, \tag{G10}$$

where $p(i \to f)$ is the change of probability for target qubit's state before and after swap operation.

The total average mutual information is the sum of the product for the probability of the corresponding event and the mutual information, that is, $\langle I\rangle = \sum_{i,f,i',f' \in \{0,1\}} P(fi; f'i')I(ff'; ii')$.

3. Generalized Jarzynski relations under the TPM protocol

Theoretically, the generalized Jarzynski relations under the TPM protocol is

$$\left\langle e^{\beta(\Delta F-W)-I}\right\rangle = \sum_{i,f,i',f'\in\{0,1\}} P(fi;f'i')e^{-\hbar\omega(f-i)-I(ff';ii')} = 1. \tag{G11}$$

For subsystem A, without considering the influence of the mutual information, there are

$$\left\langle e^{\beta(\Delta F-W_A)}\right\rangle = \sum_{i,f,i',f'\in\{0,1\}} P(fi;f'i')e^{-\Delta E_A(f-i)}. \tag{G12}$$

When ΔF is zero, the mean value of the exponential term of applied work is [5]

$$\left\langle e^{-W_\epsilon/k_BT_A}\right\rangle = \frac{2}{1+e^{-\frac{\Delta E_A}{k_BT_A}}} - 2\epsilon\tanh\left(\frac{\Delta E_A}{2k_BT_A}\right). \tag{G13}$$

Considering the influence of the mutual information and the free energy change we have

$$\left\langle e^{\beta(\Delta F-W_A)-I}\right\rangle = \sum_{\substack{i,f\\ i',f'\in\{0,1\}}} P(fi;f'i')e^{-\Delta E_A(f-i)-I(ff';ii')}.$$

Since the subsystem A is a two-dimensional array of qubits with frequency alignment at f_A, there is

$$\left\langle e^{\beta(\Delta F-W_A)}\right\rangle = \sum_{\substack{i,f\\ i',f'\in\{0,1\}}} P(fi;f'i')e^{-(f-i)\sum_{i\in\{A\}}\Delta P_i h f_A} \tag{G14}$$

and

$$\left\langle e^{\beta(\Delta F-W_A)-I}\right\rangle = \sum_{\substack{i,f\\ i',f'\in\{0,1\}}} P(fi;f'i')e^{-(f-i)\sum_{i\in\{A\}}\Delta P_i h f_A-I(ff';ii')}. \tag{G15}$$

To verify the generalized Jarzynski relations in subsystem A, we need to determine whether the experimental value of $\langle e^{\beta(\Delta F-W_A)-I}\rangle$ is around 1 or not.

APPENDIX H: QB IN MODEL OF QUANTUM SZILARD ENGINE

Our experiment of Fig. 4 is also similar to the model of the quantum Szilard engine. In this section we will discuss the Sagawa-Ueda theorem and the optimization problem in the quantum Szilard heat engine, which is helpful to understand the second law of thermaldynamics in our Maxwell's demon-type QB with only one excitation.

1. Sagawa-Ueda theorem in the Szilard engine

In our setup, the calibration process for the iSWAP-like gate could be regarded as a step of the Szilard engine in quantum version. The Szilard engine with the converted energy from the demon [99] is

$$-\langle\Delta F-W\rangle = -k_BT\left\{\ln 2+\frac{1-\epsilon}{2}\ln P_{\text{targetA}}(1) + \frac{\epsilon}{2}\ln[1-P_{\text{targetA}}(1)] + \frac{1-\epsilon}{2}\ln P_{\text{targetA}}(0) + \frac{\epsilon}{2}\ln[1-P_{\text{targetA}}(0)]\right\}. \tag{H1}$$

Now when $P_{\text{targetA}}(1)=P_{\text{targetA}}(0)=1-\epsilon$, the target qubits measurement error has been corrected perfectly, so the information is fully converted into the work:

$$-\langle\Delta F-W\rangle_{\text{ideal}} = -k_BT[\ln 2+\epsilon\ln\epsilon+(1-\epsilon)\ln(1-\epsilon)]. \tag{H2}$$

Then, when our measurement is not ideal, $P_{\text{targetA}}(1)\neq P_{\text{targetA}}(0)\neq 1-\epsilon$, there is $\langle\Delta F-W\rangle_\epsilon < \langle\Delta F-W\rangle_{\text{ideal}}$. For mutual information of a single qubit, $\langle I\rangle = \ln 2+\epsilon\ln\epsilon+(1-\epsilon)$, then in the quantum Szilard engine there is $\langle\Delta F-W\rangle \leqslant \langle I\rangle$. This theoretically verifies the Sagawa-Ueda theorem. And if we take the measure error into account, we have

$$\langle\Delta F-W_A\rangle_\epsilon = \langle\Delta F-W_A\rangle_{\epsilon=0}-\epsilon_{1\to0}\Delta E_A. \tag{H3}$$

2. Optimization of quantum Szilard heat engine

The optimization of the quantum Szilard engine is also an interesting topic, which is similar to the optimization of the iSWAP gate—both aim to move excitations to from one side to the other side. Here the Hamiltonian of the quantum Szilard engine when we splitting the wave function can be written as [100]

$$\hat{H}(t) = -\frac{\hbar^2}{2m}\frac{\partial^2 x}{x^2}+\alpha(t)f(x-d). \tag{H4}$$

The effect of the insertion moment on the potential field is $\alpha(t)$, and the effect of the insertion position on the potential field is $f(x-d)$, which is a Dirac function in the ideal case and a Gaussian-type function realistically, so the boundary conditions the wave function changes will change before and after the "insertion" step accordingly. So we get Schrödinger's equation,

$$-\frac{\hbar^2}{2m}\frac{\partial^2 x}{x^2}|\Phi(t)\rangle+\alpha(t)f(x-d)|\Phi(t)\rangle = E(t)|\Phi(t)\rangle. \tag{H5}$$

Then for a two-level quantum Szilard engine wave function containing time the solution is

$$|\Phi(t)\rangle = \sum_{n\in1,2,\ldots} c_n(t)|\Phi_n(t)\rangle e^{\frac{-iE_n(t)}{\hbar}}. \tag{H6}$$

The whole process of the wave function evolves from the initial state $\Phi(0)$ to the superposition state $|\Phi(t)\rangle$, where the work is the change of the Hamiltonian of the system as

$$W = \sum_{n\in1,2,\ldots} E_n(t)|c_n(t)|^2 - E_1(0)|c_1(0)|^2. \tag{H7}$$

Then the process of finding the optimal insertion time t to make the energy exchange as much as possible can be regarded as an optimization problem with the coefficient $|c_n(t)|^2$ of the wave function evolving to moment t. For a Maxwell's demon QB in our case, the parameters of the two-qubit iSWAP gate are equivalent to the boundary conditions and energy level of wave function in quantum Szilard engine. Then the optimized iSWAP gate and the system correspond to the maximum value of $|c_n(t)|^2$. In this condition, this quantum Szilard

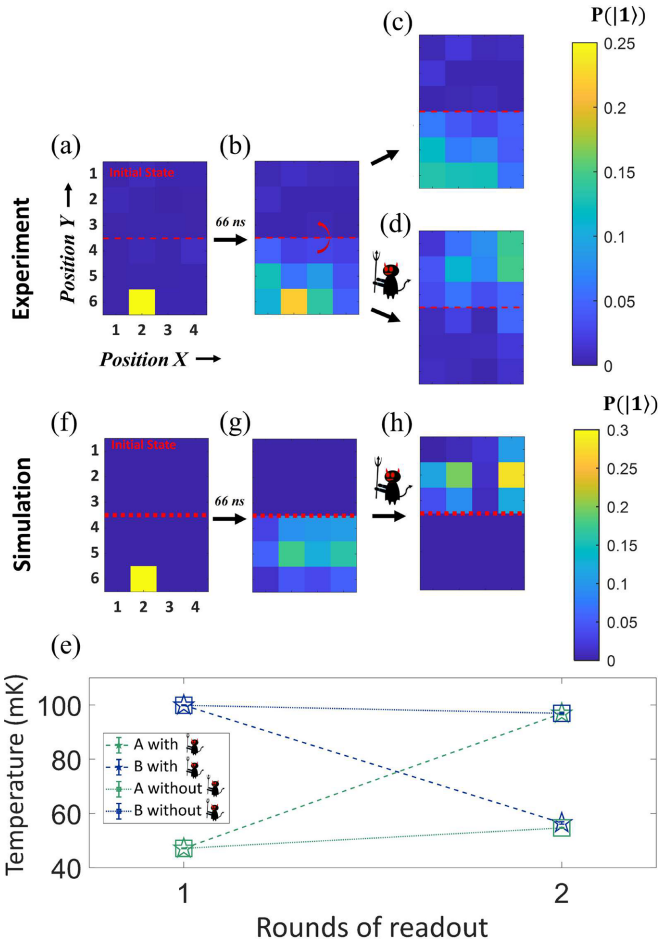

FIG. 20. Demonic effect in the single-excitation case of system 3×4 when $t_{\text{evol}} = 66$ ns. (a) The initial state preparation in the single-excitation case with the initial excitation qubit "U30Q2." (b) Qubit probability distributions of the two subsystems in the single-excitation case $t_{\text{evol}} = 66$ ns. (c, d) σ_z system measurements at $r = 2$ for system 3×4 without or with Maxwell's demon action for 3 million measurements respectively. (f–h) Simulation results corresponding to the first and second rounds of evolution of system 3×4 with the same initial setup conditions as (a), (b), and (d). (e) The effective temperature vs rounds of feedback control of each subsystem in size of 3×4 in the single excitation case.

engine is optimized to release maximum work W when the fidelity of the iSWAP gate is optimized to maximum value.

3. Demonic effects under single excitation

Figure 20 shows the transfer process of the quantum states in system 3×4 at the moment of $t_{\text{evol}} = 66$ ns. In Fig. 20 it can be observed that in Fig. 20(b), the single-excitation case of system B in round 1, the excitations are more uniformly distributed in subsystem B. Meanwhile, a small amount of thermal excitations exist in the experimental data due to thermal excitations and readout errors, which is also distributed uniformly in subsystem A because of frequency alignment. In round 2, a small amount of excitation flows naturally from system B to system A through the iSWAP-like gate in Fig. 20(c) without the feedback control, while a large amount of excitation is transferred from B to A through the Maxwell's demon swap operation selectively. Finally in Fig. 20(d), due to Maxwell's demon selection, this results in significantly more excitation in subsystem A than in subsystem B.

As shown in Fig. 20(e), the effective temperature of the subsystem is 47 mK for subsystem A and 100 mK for subsystem B at the first round. In the second round, with the effect of Maxwell's demon, the effective temperature of subsystem A is 97 mK and the effective temperature of subsystem B is 56 mK, and the temperature of system A is already higher than that of system B by 40 mK. In Fig. 20(e) we observe that the effective temperature of subsystem A is 55 mK and the effective temperature of subsystem B is 97 mK without the Maxwell's demon effect, and the effective temperature of subsystem A is obviously lower than B.

Based on the phenomena of qubit probability distribution and effective temperature variation under single excitation, we observe that the directional heat transport is significantly accelerated by Maxwell's demon within this isolated system.

4. KSE and phase space utilization of store work in the 2 × 3 and 3 × 3 subsystem

In Figs. 21(a) and 21(b) we observe that $E_{\text{KS}}\delta t$ in subsystem 2×3 still fluctuates with time due to the finite size effect, while the fluctuations of $E_{\text{KS}}\delta t$ in subsystem 3×3

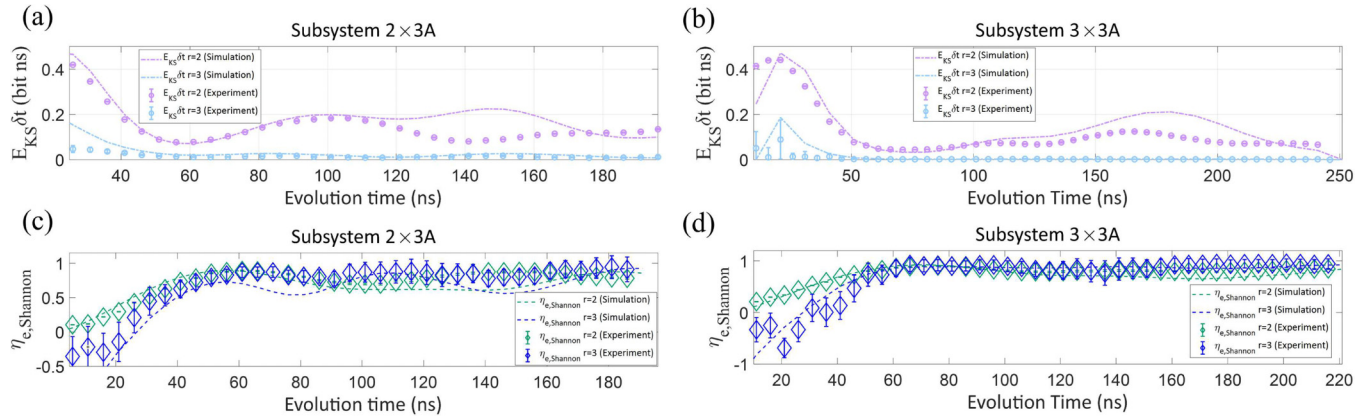

FIG. 21. Dynamical indicators of Maxwell's demon-type QB in system 2×3 and 3×3. In (a) and (b) we plot $E_{\text{KS}}\delta t$ for the subsystem 2×3A and subsystem 3×3A, respectively. In (c) and (d) we plot the stored work rate occupied in phase space η_e of subsystem 2×3A and subsystem 3×3A, respectively.

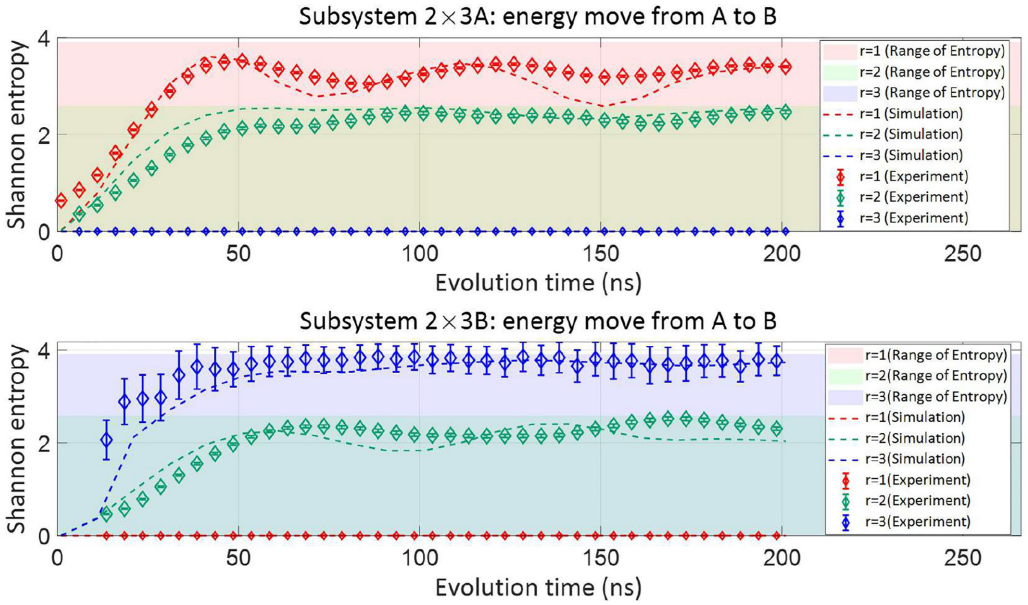

FIG. 22. Evolution of probability and entropy with the number of readout rounds for the 2×3 scale superconducting qubit system with excited state transfer from subsystem A to B. (a), (b) Simulation and experimental values of entropy evolution with time for systems 2×3 with two subsystems A and B, respectively. The number of experimental measurements and simulation points is 500 000. The initial excitation qubits are "U10Q3" and "U21Q0."

are much smaller. Both subsystems have the fluctuation of $E_{\mathrm{KS}}\delta t$ in the second round larger than the third round, that is, $\mathrm{std}(E_{\mathrm{KS,r=2}}\delta t) > \mathrm{std}(E_{\mathrm{KS,r=3}}\delta t)$.

According to the phenomena in Figs. 21(c) and 21(d), it is obvious that the stored work rate occupied in phase space of subsystem 2×3 oscillates more violently than subsystem 3×3, while the stored work rate occupied in phase space of subsystem 3×3 is always greater than 0.7 after 50 ns, and the degree of fluctuation with time is smaller than subsystem 2×3. The result suggests that if we want to pursue stability, we could choose a larger size system with a higher degree of ETH to build our Maxwell's demon-type QB.

5. Energy transfer from subsystem A to B conversely

Take the system 2×3 as an example. We use subsystem A as the initial excited system for the experiment of energy transfer from subsystem A to subsystem B.

According to the result of Shannon entropy in Fig. 22 the excitation number is successively transferred from subsystem A to subsystem B as the number of readout rounds increases. This reverse heat transport experiment can prove that the experimental zone qubit system is symmetric. For different roles of the target system/heat reservoir, there is no need for special treatment of the A/B subsystem (in other words, the QB and the charger) as a Maxwell's demon-type QB.

[1] C. G. Knott, *Life and Scientific Work of Peter Guthrie Tait* (Cambridge University Press, Cambridge, 1911), Vol. 1.

[2] R. Landauer, Irreversibility and heat generation in the computing process, IBM J. Res. Dev. **5**, 183 (1961).

[3] P. A. Camati, J. P. S. Peterson, T. B. Batalhão, K. Micadei, A. M. Souza, R. S. Sarthour, I. S. Oliveira, and R. M. Serra, Experimental rectification of entropy production by Maxwell's demon in a quantum system, Phys. Rev. Lett. **117**, 240502 (2016).

[4] M. D. Vidrighin, O. Dahlsten, M. Barbieri, M. S. Kim, V. Vedral, and I. A. Walmsley, Photonic Maxwell's demon, Phys. Rev. Lett. **116**, 050401 (2016).

[5] J. V. Koski, V. F. Maisi, T. Sagawa, and J. P. Pekola, Experimental observation of the role of mutual information in the nonequilibrium dynamics of a Maxwell demon, Phys. Rev. Lett. **113**, 030601 (2014).

[6] J. V. Koski, A. Kutvonen, I. M. Khaymovich, T. Ala-Nissila, and J. P. Pekola, On-chip Maxwell's demon as an information-powered refrigerator, Phys. Rev. Lett. **115**, 260602 (2015).

[7] M. Endres, H. Bernien, A. Keesling, H. Levine, E. R. Anschuetz, A. Krajenbrink, C. Senko, V. Vuletic, M. Greiner, and M. D. Lukin, Atom-by-atom assembly of defect-free one-dimensional cold atom arrays, Science **354**, 1024 (2016).

[8] A. Kumar, T.-Y. Wu, F. Giraldo, and D. S. Weiss, Sorting ultracold atoms in a three-dimensional optical lattice in a realization of Maxwell's demon, Nature (London) **561**, 83 (2018).

[9] N. Cottet, S. Jezouin, L. Bretheau, P. Campagne-Ibarcq, Q. Ficheux, J. Anders, A. Auffèves, R. Azouit, P. Rouchon, and B. Huard, Observing a quantum Maxwell demon at work, Proc. Natl. Acad. Sci. USA **114**, 7561 (2017).

[10] M. Naghiloo, J. J. Alonso, A. Romito, E. Lutz, and K. W. Murch, Information gain and loss for a quantum Maxwell's demon, Phys. Rev. Lett. **121**, 030604 (2018).

[11] Y. Masuyama, K. Funo, Y. Murashita, A. Noguchi, S. Kono, Y. Tabuchi, R. Yamazaki, M. Ueda, and Y. Nakamura,

Information-to-work conversion by Maxwell's demon in a superconducting circuit quantum electrodynamical system, Nat. Commun. **9**, 1291 (2018).

[12] A. V. Lebedev, G. B. Lesovik, V. M. Vinokur, and G. Blatter, Extended quantum Maxwell demon acting over macroscopic distances, Phys. Rev. B **98**, 214502 (2018).

[13] L. L. Yan, T. P. Xiong, K. Rehan, F. Zhou, D. F. Liang, L. Chen, J. Q. Zhang, W. L. Yang, Z. H. Ma, and M. Feng, Single-atom demonstration of the quantum Landauer principle, Phys. Rev. Lett. **120**, 210601 (2018).

[14] L.-L. Yan, J.-W. Zhang, M.-R. Yun, J.-C. Li, G.-Y. Ding, J.-F. Wei, J.-T. Bu, B. Wang, L. Chen, S.-L. Su *et al.*, Experimental verification of dissipation-time uncertainty relation, Phys. Rev. Lett. **128**, 050603 (2022).

[15] R. Alicki and M. Fannes, Entanglement boost for extractable work from ensembles of quantum batteries, Phys. Rev. E **87**, 042123 (2013).

[16] T. P. Le, J. Levinsen, K. Modi, M. M. Parish, and F. A. Pollock, Spin-chain model of a many-body quantum battery, Phys. Rev. A **97**, 022106 (2018).

[17] D. Rossini, G. M. Andolina, D. Rosa, M. Carrega, and M. Polini, Quantum advantage in the charging process of Sachdev-Ye-Kitaev batteries, Phys. Rev. Lett. **125**, 236402 (2020).

[18] H.-L. Shi, S. Ding, Q.-K. Wan, X.-H. Wang, and W.-L. Yang, Entanglement, coherence, and extractable work in quantum batteries, Phys. Rev. Lett. **129**, 130602 (2022).

[19] J.-Y. Gyhm, D. Šafránek, and D. Rosa, Quantum charging advantage cannot be extensive without global operations, Phys. Rev. Lett. **128**, 140501 (2022).

[20] J.-X. Liu, H.-L. Shi, Y.-H. Shi, X.-H. Wang, and W.-L. Yang, Entanglement and work extraction in the central-spin quantum battery, Phys. Rev. B **104**, 245418 (2021).

[21] G. Francica, J. Goold, F. Plastina, and M. Paternostro, Daemonic ergotropy: Enhanced work extraction from quantum correlations, npj Quantum Inf. **3**, 12 (2017).

[22] C. Elouard and A. N. Jordan, Efficient quantum measurement engines, Phys. Rev. Lett. **120**, 260601 (2018).

[23] G. Mariia, K. Michal, and F. Radim, Measurement induced synthesis of coherent quantum batteries, Sci. Rep. **9**, 19628 (2019).

[24] J.-S. Yan and J. Jing, Charging by quantum measurement, Phys. Rev. Appl. **19**, 064069 (2023).

[25] K. Liu, M. Nakagawa, and M. Ueda, Maxwell's demon for quantum transport, arXiv:2303.08326.

[26] J. M. Deutsch, Quantum statistical mechanics in a closed system, Phys. Rev. A **43**, 2046 (1991).

[27] M. Srednicki, Chaos and quantum thermalization, Phys. Rev. E **50**, 888 (1994).

[28] M. Rigol, V. Dunjko, and M. Olshanii, Thermalization and its mechanism for generic isolated quantum systems, Nature (London) **452**, 854 (2008).

[29] W. Beugeling, R. Moessner, and M. Haque, Finite-size scaling of eigenstate thermalization, Phys. Rev. E **89**, 042112 (2014).

[30] A. M. Kaufman, M. E. Tai, A. Lukin, M. Rispoli, R. Schittko, P. M. Preiss, and M. Greiner, Quantum thermalization through entanglement in an isolated many-body system, Science **353**, 794 (2016).

[31] M. Brenes, S. Pappalardi, J. Goold, and A. Silva, Multipartite entanglement structure in the eigenstate thermalization hypothesis, Phys. Rev. Lett. **124**, 040605 (2020).

[32] M. Gong, S. Wang, C. Zha, M.-C. Chen, H.-L. Huang, Y. Wu, Q. Zhu, Y. Zhao, S. Li, S. Guo *et al.*, Quantum walks on a programmable two-dimensional 62-qubit superconducting processor, Science **372**, 948 (2021).

[33] Z. Cai, R. Babbush, S. C. Benjamin, S. Endo, W. J. Huggins, Y. Li, J. R. McClean, and T. E. O'Brien, Quantum error mitigation, Rev. Mod. Phys. **95**, 045005 (2023).

[34] T. Sagawa and M. Ueda, Generalized jarzynski equality under nonequilibrium feedback control, Phys. Rev. Lett. **104**, 090602 (2010).

[35] N. Katz, M. Neeley, M. Ansmann, R. C. Bialczak, M. Hofheinz, E. Lucero, A. O'Connell, H. Wang, A. N. Cleland, J. M. Martinis, and A. N. Korotkov, Reversal of the weak measurement of a quantum state in a superconducting phase qubit, Phys. Rev. Lett. **101**, 200401 (2008).

[36] J. T. Monroe, N. Yunger Halpern, T. Lee, and K. W. Murch, Weak measurement of a superconducting qubit reconciles incompatible operators, Phys. Rev. Lett. **126**, 100403 (2021).

[37] O. Gühne, E. Haapasalo, T. Kraft, J.-P. Pellonpää, and R. Uola, Colloquium: Incompatible measurements in quantum information science, Rev. Mod. Phys. **95**, 011003 (2023).

[38] C. Elouard, D. Herrera-Martí, B. Huard, and A. Auffèves, Extracting work from quantum measurement in Maxwell's demon engines, Phys. Rev. Lett. **118**, 260603 (2017).

[39] A. Lupascu, A. Lupascu, S. L. Saito, S. L. Saito, T. Picot, P. de Groot, C. Harmans, and J. E. Mooij, Quantum non-demolition measurement of a superconducting two-level system, Nat. Phys. **3**, 119 (2007).

[40] D. Mandal and C. Jarzynski, Work and information processing in a solvable model of Maxwell's demon, Proc. Natl. Acad. Sci. USA **109**, 11641 (2012).

[41] D. Rossini, G. M. Andolina, and M. Polini, Many-body localized quantum batteries, Phys. Rev. B **100**, 115142 (2019).

[42] A. E. Allahverdyan, R. Balian, and T. M. Nieuwenhuizen, Maximal work extraction from finite quantum systems, Europhys. Lett. **67**, 565 (2004).

[43] K. Koshihara and K. Yuasa, Quantum ergotropy and quantum feedback control, Phys. Rev. E **107**, 064109 (2023).

[44] B. n. Mula, E. M. Fernández, J. E. Alvarellos, J. J. Fernández, D. García-Aldea, S. N. Santalla, and J. Rodríguez-Laguna, Ergotropy and entanglement in critical spin chains, Phys. Rev. B **107**, 075116 (2023).

[45] F. Tacchino, T. F. F. Santos, D. Gerace, M. Campisi, and M. F. Santos, Charging a quantum battery via nonequilibrium heat current, Phys. Rev. E **102**, 062133 (2020).

[46] F. Barra, Dissipative charging of a quantum battery, Phys. Rev. Lett. **122**, 210601 (2019).

[47] G. M. Andolina, M. Keck, A. Mari, M. Campisi, V. Giovannetti, and M. Polini, Extractable work, the role of correlations, and asymptotic freedom in quantum batteries, Phys. Rev. Lett. **122**, 047702 (2019).

[48] A. Kowalewska-Kudłaszyk, J. Kalaga, W. Leoński, and V. Cao Long, Kullback–Leibler quantum divergence as an indicator of quantum chaos, Phys. Lett. A **376**, 1280 (2012).

[49] V. Balasubramanian, P. Caputa, J. M. Magan, and Q. Wu, Quantum chaos and the complexity of spread of states, Phys. Rev. D **106**, 046007 (2022).
[50] P. Caputa, J. M. Magan, and D. Patramanis, Geometry of Krylov complexity, Phys. Rev. Res. **4**, 013041 (2022).
[51] E. B. Rozenbaum, S. Ganeshan, and V. Galitski, Lyapunov exponent and out-of-time-ordered correlator's growth rate in a chaotic system, Phys. Rev. Lett. **118**, 086801 (2017).
[52] J. M. R. Parrondo, J. M. Horowitz, and T. Sagawa, Thermodynamics of information, Nat. Phys. **11**, 131 (2015).
[53] S. Toyabe, T. Sagawa, M. Ueda, E. Muneyuki, and M. Sano, Experimental demonstration of information-to-energy conversion and validation of the generalized Jarzynski equality, Nat. Phys. **6**, 988 (2010).
[54] S. W. Kim, T. Sagawa, S. De Liberato, and M. Ueda, Quantum Szilard engine, Phys. Rev. Lett. **106**, 070401 (2011).
[55] K. L. Viisanen, S. Suomela, S. Gasparinetti, O.-P. Saira, J. Ankerhold, and J. P. Pekola, Incomplete measurement of work in a dissipative two level system, New J. Phys. **17**, 055014 (2015).
[56] M. Perarnau-Llobet, E. Bäumer, K. V. Hovhannisyan, M. Huber, and A. Acin, No-go theorem for the characterization of work fluctuations in coherent quantum systems, Phys. Rev. Lett. **118**, 070601 (2017).
[57] K. Micadei, G. T. Landi, and E. Lutz, Quantum fluctuation theorems beyond two-point measurements, Phys. Rev. Lett. **124**, 090602 (2020).
[58] M. H. Mohammady, Self-consistency of the two-point energy measurement protocol, Phys. Rev. A **103**, 042214 (2021).
[59] J. M. Horowitz and J. M. R. Parrondo, Thermodynamic reversibility in feedback processes, Europhys. Lett. **95**, 10005 (2011).
[60] G. Paneru, S. Dutta, T. Sagawa, T. Tlusty, and H. K. Pak, Efficiency fluctuations and noise induced refrigerator-to-heater transition in information engines, Nat. Commun. **11**, 1012 (2020).
[61] T. P. Xiong, L. L. Yan, F. Zhou, K. Rehan, D. F. Liang, L. Chen, W. L. Yang, Z. H. Ma, M. Feng, and V. Vedral, Experimental verification of a Jarzynski-related information-theoretic equality by a single trapped ion, Phys. Rev. Lett. **120**, 010601 (2018).
[62] W. Liu, Z. Niu, W. Cheng, X. Li, C.-K. Duan, Z. Yin, X. Rong, and J. Du, Experimental test of the Jarzynski equality in a single spin-1 system using high-fidelity single-shot readouts, Phys. Rev. Lett. **131**, 220401 (2023).
[63] K. Micadei, J. P. Peterson, A. M. Souza *et al.*, Reversing the direction of heat flow using quantum correlations, Nat. Commun. **10**, 2456 (2019).
[64] G. Francica, F. C. Binder, G. Guarnieri, M. T. Mitchison, J. Goold, and F. Plastina, Quantum coherence and ergotropy, Phys. Rev. Lett. **125**, 180603 (2020).
[65] M. B. Arjmandi, A. Shokri, E. Faizi, and H. Mohammadi, Performance of quantum batteries with correlated and uncorrelated chargers, Phys. Rev. A **106**, 062609 (2022).
[66] M. Hadipour, S. Haseli, H. Dolatkhah, and M. Rashidi, Study the charging process of moving quantum batteries inside cavity, Sci. Rep. **13**, 10672 (2023).
[67] K. Bharti, A. Cervera-Lierta, T. H. Kyaw, T. Haug, S. Alperin-Lea, A. Anand, M. Degroote, H. Heimonen, J. S. Kottmann, T. Menke *et al.*, Noisy intermediate-scale quantum algorithms, Rev. Mod. Phys. **94**, 015004 (2022).
[68] D. A. Abanin, E. Altman, I. Bloch, and M. Serbyn, Colloquium: Many-body localization, thermalization, and entanglement, Rev. Mod. Phys. **91**, 021001 (2019).
[69] C. J. Neill, P. Roushan, M. T. Fang, Y. Chen, M. H. Kolodrubetz, Z. Chen, A. Megrant, R. Barends, B. Campbell, B. Chiaro *et al.*, Ergodic dynamics and thermalization in an isolated quantum system, Nat. Phys. **12**, 1037 (2016).
[70] N. Freitas and M. Esposito, Maxwell demon that can work at macroscopic scales, Phys. Rev. Lett. **129**, 120602 (2022).
[71] H. T. Quan, Y. D. Wang, Y.-X. Liu, C. P. Sun, and F. Nori, Maxwell's demon assisted thermodynamic cycle in superconducting quantum circuits, Phys. Rev. Lett. **97**, 180402 (2006).
[72] C. Y. Cai, H. Dong, and C. P. Sun, Multiparticle quantum Szilard engine with optimal cycles assisted by a Maxwell's demon, Phys. Rev. E **85**, 031114 (2012).
[73] M. A. Nielsen, C. M. Caves, B. Schumacher, and H. Barnum, Information-theoretic approach to quantum error correction and reversible measurement, Proc. R. Soc. London A **454**, 277 (1998).
[74] A. Rex, Maxwell's demon—A historical review, Entropy **19**, 240 (2017).
[75] P. Sartori and S. Pigolotti, Thermodynamics of error correction, Phys. Rev. X **5**, 041039 (2015).
[76] J. Bricmont, K. Gawedzki, and A. Kupiainen, Kam theorem and quantum field theory, Commun. Math. Phys. **201**, 699 (1999).
[77] G. P. Brandino, J.-S. Caux, and R. M. Konik, Glimmers of a quantum Kam theorem: Insights from quantum quenches in one-dimensional Bose gases, Phys. Rev. X **5**, 041043 (2015).
[78] O. A. Castro-Alvaredo, B. Doyon, and T. Yoshimura, Emergent hydrodynamics in integrable quantum systems out of equilibrium, Phys. Rev. X **6**, 041065 (2016).
[79] V. Alba, Entanglement and quantum transport in integrable systems, Phys. Rev. B **97**, 245135 (2018).
[80] F. Arute *et al.*, Quantum supremacy using a programmable superconducting processor, Nature (London) **574**, 505 (2019).
[81] R. Barends, C. M. Quintana, A. G. Petukhov, Y. Chen, D. Kafri, K. Kechedzhi, R. Collins, O. Naaman, S. Boixo, F. Arute *et al.*, Diabatic gates for frequency-tunable superconducting qubits, Phys. Rev. Lett. **123**, 210501 (2019).
[82] Z. Ni, S. Li, X. Deng, Y. Cai, L. Zhang, W. Wang, Z.-B. Yang, H. Yu, F. Yan, S. Liu *et al.*, Beating the break-even point with a discrete variable-encoded logical qubit, Nature (London) **616**, 56 (2023).
[83] A. Vepsäläinen, R. Winik, A. H. Karamlou, J. Braumüller *et al.*, Improving qubit coherence using closed-loop feedback, Nat. Commun. **13**, 1932 (2022).
[84] W. P. Livingston, M. S. Blok, E. Flurin, J. Dressel, A. N. Jordan, and I. Siddiqi, Experimental demonstration of continuous quantum error correction, Nat. Commun. **13**, 2307 (2022).
[85] J. Freericks and H. Monien, Phase diagram of the Bose-Hubbard model, Europhys. Lett. **26**, 545 (1994).
[86] Y. Yanay, J. Braumüller, S. Gustavsson, W. D. Oliver, and C. Tahan, Two-dimensional hard-core Bose–Hubbard model with superconducting qubits, npj Quantum Inf. **6**, 58 (2020).
[87] A. van Otterlo, K.-H. Wagenblast, R. Baltin, C. Bruder, R. Fazio, and G. Schön, Quantum phase transitions of interacting

bosons and the supersolid phase, Phys. Rev. B **52**, 16176 (1995).

[88] Y. Ye, Z.-Y. Ge, Y. Wu, S. Wang, M. Gong, Y.-R. Zhang, Q. Zhu, R. Yang, S. Li, F. Liang *et al.*, Propagation and localization of collective excitations on a 24-qubit superconducting processor, Phys. Rev. Lett. **123**, 050502 (2019).

[89] B. Bhattacharjee, P. Nandy, and T. Pathak, Krylov complexity in large q and double-scaled SYK model, J. High Energy Phys. 08 (2023) 099.

[90] Ya. B. Pesin, Characteristic Lyapunov exponents and smooth ergodic theory, Russ. Math. Surv. **32**, 55 (1977).

[91] A. Hallam, J. Morley, and A. Green, The Lyapunov spectra of quantum thermalisation, Nat. Commun. **10**, 2708 (2019).

[92] T. Goldfriend and J. Kurchan, Quantum Kolmogorov-Sinai entropy and Pesin relation, Phys. Rev. Res. **3**, 023234 (2021).

[93] V. Lecomte, Thermodynamic formalism for systems with Markov dynamics, J. Stat. Phys. **127**, 51 (2007).

[94] O. Schnaack, N. Bölter, S. Paeckel, S. R. Manmana, S. Kehrein, and M. Schmitt, Tripartite information, scrambling, and the role of Hilbert space partitioning in quantum lattice models, Phys. Rev. B **100**, 224302 (2019).

[95] M. Rigol, V. Dunjko, V. Yurovsky, and M. Olshanii, Relaxation in a completely integrable many-body quantum system: An *ab initio* study of the dynamics of the highly excited states of 1D lattice hard-core bosons, Phys. Rev. Lett. **98**, 050405 (2007).

[96] G. Biroli, C. Kollath, and A. M. Läuchli, Effect of rare fluctuations on the thermalization of isolated quantum systems, Phys. Rev. Lett. **105**, 250401 (2010).

[97] A. Piga, M. Lewenstein, and J. Q. Quach, Quantum chaos and entanglement in ergodic and nonergodic systems, Phys. Rev. E **99**, 032213 (2019).

[98] G. Zhu, D. G. Ferguson, V. E. Manucharyan, and J. Koch, Circuit QED with fluxonium qubits: Theory of the dispersive regime, Phys. Rev. B **87**, 024510 (2013).

[99] T. Sagawa and M. Ueda, Nonequilibrium thermodynamics of feedback control, Phys. Rev. E **85**, 021104 (2012).

[100] V. B. Sørdal and J. Bergli, Deep reinforcement learning for quantum Szilard engine optimization, Phys. Rev. A **100**, 042314 (2019).